Late Quaternary faulting on the Manas and Hutubi reverse faults in the northern foreland basin of Tian Shan, China

Zhijun Gong[a,b], Sheng-Hua Li[b,*], Bo Li[b,c]

[a] Key Laboratory of Cenozoic Geology and Environment, Institute of Geology and Geophysics, Chinese Academy of Sciences, Beijing, China

[b] Department of Earth Sciences, The University of Hong Kong, Pokfulan Road, Hong Kong, China

[c] Centre for Archaeological Science, School of Earth and Environmental Sciences, University of Wollongong, Wollongong, NSW 2522, Australia

* Corresponding author. Email: shli@hku.hk

Abstract:

The Tian Shan Range lies in the actively deforming part of the India–Asia collision zone. In the northern foreland basin of Tian Shan, the strata were intensively deformed by Cenozoic folding and faulting. Slip rate studies along these faults are important for understanding the dynamics of crustal deformation and evaluating the seismic hazards in the region. Two reverse faults (the Manas and Hutubi faults) in the northern foreland basin were investigated. Due to past faulting events along these faults, the terrace treads along the Manas River were ruptured, forming fault scarps several meters in height. Loess deposits were trapped and preserved at the surface ruptures along these scarps. The thickness of the trapped loess is dependent on the size of the ruptures. The minimum and maximum ages of these scarps are constrained by dating the loess preserved at the surface ruptures and the terrace treads, respectively, using the quartz optically stimulated luminescence (OSL) dating technique. Our dating results suggest that the loess trapped at the ruptures was deposited from the early to mid-Holocene at the Hutubi Fault, and from the mid- to late-Holocene at the Manas Fault. The vertical displacements of the faults were evaluated by measuring the topographic profiles across the investigated fault scarps using the differential global position system (DGPS). Our results suggest that, during the late Quaternary in the studied region, the vertical slip rates of the Manas Fault were between ~0.74 mm/yr and ~1.6 mm/yr, while the Hutubi Fault had a much lower vertical slip rate between ~0.34 mm/yr and ~0.40 mm/yr. The tectonic implications of our results are discussed.

Keywords: Tian Shan, Reverse fault, OSL dating, loess, DGPS

1. Introduction

In response to the Cenozoic collision of the Indian and Eurasian continental plates, Tian Shan has been one of the most active intra-continental mountain building belts in Central Asia (Fig. 1(a)) (Molnar and Tapponnier, 1975; Tapponnier and Molnar, 1979; Avouac et al., 1993; Fu et al., 2003; Sun and Zhang, 2009). The folded Cenozoic deposits in the foreland basins of Tian Shan indicate active tectonics and crustal thickening during the Cenozoic era (Sun and Zhang, 2009). Previous studies suggested that crustal shortening in the Tian Shan region can be up to 200 ± 50 km and that the average altitude of Tian Shan has been uplifted to more than 4000 m (Avouac et al., 1993; Abdrakhmatov et al., 1996; Deng et al., 1996).

In recent years, cities such as Urumqi in the northern foreland basin of Tian Shan have been developing rapidly. However, the cities are threatened by a number of major active fault systems. Several significant surface-rupturing earthquakes have occurred in the region during historical times, including the 1906 M=7.7 Manas earthquake at Manas town. During the last twenty years, there are reports on paleo-seismicity along the major active reverse faults in the northern foreland basin of Tian Shan (Fig. 1(b)) (e.g. Avouac et al., 1993; Deng et al., 1996). However, many problems remain in deciphering the timing and recurrence intervals of faulting events in the area, because there is a lack of reliable age constrains for fault movement. One way to evaluate seismic hazards in the region is to study the slip rate along the faults. Although different fault systems in the northern foreland basin of Tian Shan have been identified and studied in previous studies, such as the dip of the faults, the strike of the faults as well as the fault displacements (Xu et al., 1992; Avouac et al., 1993; Deng et al., 1996; Zhao et al., 2001), the late Quaternary slip rates along the major fault systems in the studied region are still poorly constrained, mainly due to the lack of reliable chronological data.

Optically stimulated luminescence (OSL) dating determines the time since mineral

grains were last exposed to sunlight, and hence, it can provide a direct measure of the depositional ages of fault-related sediments. OSL dating is well-suited to date sediments such as loess and sand deposits that were deposited within the last several hundred thousand years (e.g. Aitken, 1998; Wang et al., 2006; Rhodes, 2011; Li et al., 2014). It has been applied to many aeolian-related sedimentary sequences, e.g. sandy deposits from deserts in northeast China and loess deposits from Chinese Loess Plateau (e.g. Li et al., 2002; Sun et al., 2006; Li et al., 2007; Li and Li, 2011; Fu et al., 2012; Li et al., 2012; Gong et al., 2013). OSL dating has also been applied to study the faulting at different fault zones (e.g. Chen et al., 1999; Cheong et al., 2003; Nogueira et al., 2010; Chen et al., 2012, 2013).

The timing of past faulting events can be deciphered by dating fault-related colluvial sediment (e.g. Forman et al., 1991; Deng et al., 1996). However, luminescence dating of scarp-derived colluvial deposits is difficult and can be problematic because these materials might be insufficiently bleached prior to deposition, due to short transportation distances. Instead of dating the colluvial deposits, in this study, we propose that the ages of scarps may be constrained by dating the loess trapped at the surface ruptures along the fault scarps and the terrace treads, respectively. A single-aliquot regenerative-dose (SAR) OSL dating technique (Murray and Wintle, 2000) is used. Together with high-resolution differential global position system (DGPS) measurements on the fault scarps, the vertical slip rates of the two reverse faults (the Manas and Hutubi faults) are evaluated and their tectonic implications are discussed.

2 .Geological setting

In northwestern China, the Tian Shan Range separates the Tarim Basin to the south from the Junggar Basin to the north (Fig. 1(a)). The Chinese Tian Shan extends east-west more than 1700 km with a north-south width of 250-300 km (Fu et al., 2003). Cenozoic folding and faulting in the Tian Shan Range resulted in strong deformation of the Mesozoic to Cenozoic strata in the foreland basins (Fu et al., 2003; Zhang, 2004; Charreau et al., 2005; 2009; Heermance et al., 2007; Sun and Zhang, 2009; Lu et al., 2010). During the late Cenozoic, three approximately east-west striking, sub-parallel

zones of folding (I, II and III in Fig.1(b)) and reverse faulting were formed in the northern foreland basin of Tian Shan (Deng et al., 1996; Burchfiel et al., 1999; Fu et al., 2003).

In zone I, the Qingshuihe (QSH) and Qigu (QG) anticlines are composed of Mesozoic to Cenozoic strata (Fig. 1(b)). In zone II, the Huoerguosi (HGS), Manas (MNS) and Tugulu (TGL) anticlines consist of Oligocene to Pleistocene strata. In zone III, the Dushanzi (DSZ) and Anjihai (AJH) anticlines consist of Miocene to Pleistocene strata (Sun and Zhang, 2009). All the three anticlines are characterized by linear and approximately west-east striking axes, indicating a north-south contraction of the range (Xu et al., 1992; Deng et al., 1996). It was reported that zone I of such fold systems was not active during the late Quaternary, while the reverse faults in zone II and III were active during the late Quaternary (Deng et al., 1996). In this study, we focused on two reverse faults (the Hutubi and Manas faults) within the Manas Anticline in zone II (Fig. 1(b)).

Field-based investigation and satellite observations reveal that the Hutubi Fault extends roughly east to west for more than 60 km. Avouac et al. (1993) investigated the outcrops of the Hutubi Fault at the Taxi and Hutubi rivers, respectively (Fig. 1(b)). It is found that the Hutubi Fault dips 50~60° S at the Taxi River site and 50° S at the Hutubi River site. Therefore, it is very likely that the Hutubi Fault dips at a similar angle near the surface at the Manas River. The Manas Fault is approximately 2 km north of the west side of the Hutubi Fault, striking in a similar direction for more than 30 km (Fig. 1(b)). Zhao et al. (2001) investigated the shallow crustal structure characteristics of the Manas Anticline in the Manas earthquake area using a high-precision shallow seismic prospecting method. It is found that the Manas Fault dips ~45° S near the surface (Zhao et al., 2001).

The Manas River originates from Tian Shan and it flows northward to the Junggar Basin (Fig. 1(b)). Both the Manas and Hutubi faults extend across the Manas River, deforming fluvial terraces of the Manas River (Fig. 2(a),(b)). Six fluvial terraces were identified along the east bank of the Manas River within the Manas Anticline. These terraces - from the lowest to the highest - are referred as T-1 to T-6, respectively (Fig.

2(b)). The luminescence chronology for the terrace sequence has been established by dating the underlying fluvial sand and the overlying aeolian loess on the terraces (Gong et al., 2014). The ages of the six terrace treads were dated at ~ 0.5 ka, ~1.4 ka, ~3.1 ka, ~4.0 ka, ~12.4 ka and ~19.9 ka, respectively (Table 1) (Gong et al., 2014). For the six terraces, fluvial gravels are overlying Tertiary bedrocks and gravels are mantled by aeolian loess with different thicknesses ranging from around 10 cm to over 10 m. Field investigation suggests that fluvial gravels of terraces T-5 and T-6 along the Manas River were ruptured, forming fault scarps several meters in height (Fig. 2(a),(b)). Loess deposits were trapped and preserved at the surface ruptures along the scarps and the thickness of the loess trapped is variable and depends on the size of the ruptures.

The annual precipitation in the study area is less than 300 mm/yr and the precipitation is concentrated during the spring and summer months (Poisson and Avouac, 2004). The prevailing winds of the region are westerlies (Poisson and Avouac, 2004), with the area being mainly controlled by strong near-surface north and northwest winds (Fang et al., 2002; Sun, 2002). Under such winds, aeolian loess entrained from the Junggar Basin is transported and accumulates along the northern piedmont of Tian Shan (Fig. 3).

3. Surface ruptures along the reverse fault scarps

To study the faulting along the Hutubi and Manas faults, six exposures for surface ruptures along the reverse fault scarps were investigated. The locations of the exposures and their locations in relation to the two reverse faults are shown in Fig. 4(a),(b),(c). The exposures are termed as HTB0, HTB1 and MNS1-MNS4, respectively.

HTB0 (N 44° 10′ 5.1″, E 86° 08′ 11.9″) is located at the western part of the Hutubi Fault (Fig. 1(b)). It belongs to the outcrop of the Hutubi Fault at T-6 on the east bank of the Manas River (Fig. 5(a)). The gravel layer of T-6 was displaced vertically by the fault for about 7.8 m (Fig. 5(a)). Due to the development of a gully along the fault, the original scarp was destroyed so we could not find associated trapped loess on the fault scarp.

HTB1 (N 44° 10′ 11.1″, E 86° 07′ 37.7″) is the surface rupture of the terrace tread of T-5 on the east bank of the Manas River (Fig. 4(b)). It belongs to the outcrop of the Hutubi Fault at the west side. It is a part of the fault scarp, where the aeolian loess

deposits were trapped and preserved (Fig. 4(c)). The loess trapped at the rupture along the fault scarp is about 1.8 m in thickness (Fig. 5(b)).

MNS1 (N 44° 11′ 17.6″, E 86° 08′ 16.8″) is the surface rupture of the terrace tread of T-5 on the east bank of the Manas River (Fig. 4(b)) and it belongs to the outcrop of the Manas Fault (Fig. 5(c))). MNS1 is at approximately 2 km north of HTB1. The exposure is only part of the scarp of the Manas Fault, which was previously studied by Avouac et al. (1993) and Deng et al. (1996). The strata in the hanging wall of the scarp consist of Tertiary gray, gray-green and reddish deformed mudstones and the late Pleistocene gravels (Xu et al, 1992). At the foot wall, only the late Pleistocene gravels were exposed. MNS1 shows complex slope morphology and the trapped loess at the surface rupture along the scarp is about 1 m in thickness (Fig. 5(c))).

MNS2 (N 44° 11′ 18.7″, E 86° 07′ 58.3″) (Fig. 5(d)) is at about ~300 m west of MNS1 (Fig. 4(b)). The exposure also shows the surface rupture of the terrace tread of T-5 on the east bank of the Manas River, and it belongs to the outcrop of the Manas Fault (Fig. 5(d))). The trapped loess at the rupture along the fault scarp is about 1 m in thickness.

MNS3 (N 44° 11′ 27.5″, E 86° 08′ 53.18″) is shown in Fig. 5(e). It is parallel to exposures MNS1 and MNS2. This exposure is the surface rupture of the terrace tread of T-5 on the west bank of the Manas River, and it belongs to the outcrop of the Manas Fault. The trapped loess at the rupture along the fault scarp is about 1 m in thickness.

MNS4 (N 44° 11′ 27.7″, E 86° 06′ 51.8″) is shown in Fig. 5(f). It is the surface rupture of the terrace tread of T-5 on the west bank of the Manas River. MNS4 is about 100 m west of MNS3. MNS4 is a part of the scarp of the Manas Fault, where loess deposits were trapped and preserved. The loess trapped at the rupture along the scarp is about 1 m in thickness.

The scarps of the Manas and Hutubi faults extend more than tens of meters so it is very difficult to dig a trench to fully reveal the strata along these scarps. From the above exposures (HTB1, MNS1-MNS4), it is found that the hanging and foot walls along the fault scarp are composed of fluvial gravels, which are rather weakly consolidated. The fault-scarp-derived colluvial gravels have been mixed well with the hanging and foot walls

at the ruptures and their boundary are obscured. Thus, it is very difficult to distinguish individual faulting events by lithofacies analysis of colluvial sediments at these ruptures. Alternatively, trapped loess was commonly preserved at the ruptures along the fault scarps. We think the trapped loess at the surface ruptures along the fault scarps may provide important chronological information linked to past faulting events.

We follow Avouac et al's. (1993) method to estimate the fault displacements for both reverse faults, i.e. the vertical displacements of the faults were evaluated by measuring the topographic profiles across the scarps using the differential global position system (Real Time Kinematic) (Fig. 4(b)). The terrace treads of T-5 and T-6 were used as the offset markers for the faulting along the Hutubi and Manas faults and the elevation data were recorded by DGPS measurements along the cross-sections B-B′, C-C′ and D-D′(Fig. 4(b)). For our field measurements, the topographic profiles B-B′, C-C′ and D-D′ were measured long enough to cross the faulted terrace treads at either side of the scarps until the surface was nearly planar and there was no significant degradation. In addition, it was found that the regional slope of the fluvial terraces was very small (typically at 1-2°) at either side of scarps studied (estimated from Google Earth). Thus, the measured vertical offset is nearly equal to the vertical throw on the fault, independent of fault dip, as suggested by Avouac et al. (1993). The vertical displacement by the fault can be estimated by the difference in the elevations between the faulted terrace treads at either side of the scarps. We assigned a 10 % error for the fault displacements for both reverse faults. The vertical displacements along the Manas and Hutubi faults were shown in Fig. 4(b) and Fig. 5(a). It was found that the Hutubi Fault has vertically displaced terrace T-5 by 4.2 ± 0.4 m (cross-section B-B′, Fig. 4(b)) and terrace T-6 by 7.8 ± 0.8 m (cross-section C-C′, Fig. 5(a)). The Manas Fault has vertically displaced T-5 by 9.2 ± 0.9 m (cross-section D-D′, Fig. 4(b)). The cross-section (D-D′) is at the middle site between MNS1 and MNS2. Our displacement measurement results are consistent with those from Avouac et al. (1993).

4. The relationship between loess at the ruptures and faulting along the faults

To explain why the ages of the loess deposits preserved at the surface ruptures can be used to constrain the minimum ages of scarps, a schematic model is provided in Fig. 6 to

illustrate the evolution of ruptures along the fault scarp on the terrace and the infilling of loess deposits along the ruptures.

The river terrace was formed at time (t0) when the fluvial gravels were deposited on the bedrock (Fig. 6, stage 1). The terrace tread can be used as the offset marker for the faulting along the reverse fault. When a faulting event occurred (referred to as event 1) at time t1, the terrace tread was deformed and a fresh rupture was created. As the gravels from the hanging wall are weakly consolidated, they soon collapse and fill in the ruptures, forming a colluvial unit (C) (Fig. 6, stage 2). The rupture then started to trap aeolian loess deposits (L1) until a balance between deposition and erosion (Fig. 6, stage 3) was achieved. Assuming that the loess deposited soon after the surface rupture was formed, the age (t1′) of the loess layer 1 (L1) is close to the time of faulting event 1 (t1). A similar process has been documented by the reverse fault induced San Fernando earthquake of 1971 (Kahle, 1975). In that case, the hanging-wall was weakly consolidated Tertiary sandstone and conglomerate. More than 50% of the 0.3 m to 1 m high overhanging free face collapsed after three months.

When a second faulting event (event 2) occurred along the reverse fault at time t2, the hanging wall was further displaced above the foot wall, leading to the rupture growth (Fig. 6, stage 4). At this time, some surface soil (S) or loess at the rupture might be reworked and re-deposited on the foot wall block. Then, the reworked soil or loess might be eroded away, or mixed with new aeolian loess deposits (L2) to be trapped in the rupture (Fig. 6, stage 5) until a new balance reached (Fig. 6, stage 6). Such faulting and loess infilling in the rupture along the scarp was repeated, which created different loess layers. Thus, the oldest loess deposits trapped in the rupture can be used to constrain the minimum ages of scarps.

It should be noted that, an important assumption must be made for using the trapped loess deposits at the surface ruptures along the fault scarps to infer the minimum ages — that is there was a continuous loess deposition during the fault movement period. This assumption is expected to be valid for this study area. The Junggar Desert is located at the north of Tian Shan, occupying an area of 48,800 km^2 (Sun, 2002). Such a desert serves as a huge and constant holding area for aeolian dust. Besides, the study area is mainly

controlled by strong near-surface north-west and north winds (Sun, 2002). Under such winds, aeolian loess entrained from the Junggar Basin is transported and accumulates in the northern piedmont of Tian Shan - the upper limit of loess depositions can be at 2400 m above sea level (Fig. 3). Gong et al. (2014) demonstrated that there were continuous loess depositions on the terraces from ~20 ka to ~0.5 ka in the same study area. In other mountain belts of Asia, such as the Qilian Shan, it is also demonstrated that there was continuous loess deposition along the mountain front during the Holocene (e.g. Stokes et al., 2003; Küster et al., 2006). Thus, the aeolian dusts transported from the Junggar Desert to the northern piedmont of Tianshan (Sun, 2002) were very likely to be trapped at the surface ruptures and the loess deposits offer the possibility to constrain minimum ages of the scarps along the Hutubi and Manas faults in the study area.

Based on the model described above, multiple samples were collected from each of the scarps. The detailed sampling name, material and positions for the loess deposits at the ruptures along the fault scarps are shown in Table 2 and Fig. 5.

5. Luminescence dating

5.1 Experimental procedure

The OSL samples were collected by hammering stainless steel tube horizontally into freshly cut vertical sections. These tubes were then covered with a lid soon after taking them from the section, then sealed in a black plastic bag. The OSL samples were analysed in the Luminescence Dating Laboratory at the Department of Earth Science of the University of Hong Kong. Two centimeters of material at each end of the tube was scrapped away and used for dose rate measurements. Raw samples in the centre of the tubes were first treated with 10% hydrochloric acid (HCl) and 10% hydrogen peroxide (H_2O_2) to remove carbonates and organic materials, respectively. Coarse grains between 90 and 125μm were selected by mechanical dry sieving. Quartz grains were separated using sodium polytungstate heavy liquid with density between 2.62-2.75 g/cm^3. The quartz grains were etched with 40% HF for ~80 minutes to remove the outer alpha dosed layer as well as any remaining feldspar. HCl (10%) was used again to dissolve any residual fluorides after etching before final rinsing and drying. The etched grains were

mounted as a monolayer on 9.8 mm wide aluminum discs using silicone oil as an adhesive. Grains covered the central ~3 mm diameter portion of each disc, corresponding to several hundreds of grains per aliquot. The purity of the quartz grains was tested by monitoring the presence of feldspar by measuring the infrared stimulated luminescence (IRSL) and 110 °C thermoluminescence (TL) peak (Li et al., 2002). At least twenty aliquots were measured for each sample.

OSL signals were measured using automated Risø TL/OSL readers equipped with excitation units of blue light emitting diodes (LEDs) (Δ=470±30 nm) and infrared LEDs (Δ=870 ± 40nm). The blue LEDs deliver ~50 mW/cm^2 of light to the sample (Bøtter-Jensen et al., 2003). Ninety percent of their full powers were used for stimulation in this study. The quartz OSL signals were detected through 7.5 mm Hoya U-340 filters, which allow a transmission from 290 nm to 370 nm with a peak at ~340 nm (Aitken, 1998). Irradiation was carried out using ^{90}Sr/^{90}Y beta sources built into the readers.

The equivalent doses (D_e) of quartz were determined using a SAR OSL dating protocol (Wintle and Murray, 2000). In the protocol, preheating condition was determined from a preheat plateau test on the sample MNS2-4, using preheat temperatures from 200 °C to 300 °C in increments of 20 °C (Fig. 7). A D_e plateau was observed between 220 °C and 260 °C. Based on the preheat plateau results, a preheating at 220 °C for 10 s and a cut-heat at 180 °C were selected before the regenerative dose and test dose OSL measurements, respectively. Additionally, a zero dose was used for monitoring recuperation effects and a repeated dose the same as the first regeneration dose was used for checking the reproducibility of the sensitivity correction (i.e. recycling ratio). Aliquots with recuperation higher than 5% or recycling ratio falling out of the range of 1.0 ± 0.1 were discarded for age calculation.

5.2 Dose rate measurements

The environmental dose rate was determined using a variety of techniques. The Thick-source alpha counting technique (Aitken, 1998) was used to measure the dose contributions from the uranium (U) and thorium (Th) decay chains. A Littlemore 7286

TSAC system with 42-mm-diameter ZnS screens was used. Potassium content was measured by X-ray fluorescence (XRF). Water content was calculated as the ratio of water weight to dried sample weight, obtained from the sample weights before and after drying at 105 °C in an oven. As the water content may have changed through time, a 20% relative standard error was assigned for the measured water content to take account of the long-term variation in water content (refer to Table 2). The cosmic ray contribution to the dose rate was calculated from the burial depth, altitude, latitude and longitude of the samples (Prescott and Hutton, 1994). The dosimetry data were summarized in Table 2.

5.3 OSL dating results

Typical OSL shine down curves and the regenerative growth curves of quartz grains from the loess samples are shown in Figure 8. It shows that the OSL contains a strong fast component, with the OSL emission decreasing by ~80-90% during the first 4 s of stimulation. The D_e distribution from each sample was analyzed using radial plot, which has been widely used to show the distributions of single-grain or single-aliquot D_e estimations (Galbraith et al., 1999; Olley et al., 1999; Jacobs et al., 2003; Zhang et al., 2009). Fig. 9 displays examples of radial plots for six loess samples from the five exposures (HTB1 and MNS1-MNS4). In the plots, the central lines of the shaded regions with 2 σ width of the D_e distribution represent the mean D_e values of the measured aliquots. Based on the radial plots, there is no evidence of variable bleaching for these loess samples, i.e. most of the D_e values are symmetrically distributed around the central values. We conclude that our OSL ages are reliable based on the following aspects: 1) the loess deposits are aeolian in origin and are therefore unlikely to suffer from insufficient bleaching problems in OSL dating - this is supported by the D_e distribution of our samples (Fig. 9). 2) our samples yield good results in the SAR performance tests, in terms of pre-heat plateau, recycling ratio and recuperation. 3) most of the samples yield over-dispersion (OD) values between 10% and 35% (Table 3). Although the effect of inhomogeneous gamma radiation might make some contributions to the scatter of D_e, Gong et al. (2014) demonstrated that the uncertainty from spatially heterogeneous dose rates to the final age estimation is less than 5% for the OSL samples in the same study

area.

Table 3 summarizes the D_e estimates and the OSL ages of all the samples based on mean age and the central age models, respectively. It is found that the two age models produce consistent ages within 2σ for all the samples. The mean age model was chosen for final determination of the OSL ages. Fig. 10 shows the five exposures of the fault scarps together with the OSL dating results of the loess samples. The trapped loess preserved at HTB1 produced OSL ages from ~10.5 ka to ~4.2 ka. It is found that the inner trapped loess produced older ages than the outer trapped loess. In comparison, the trapped loess preserved along the Manas Fault (MNS1-MNS4) produced younger OSL ages, ranging from ~5.7 ka to ~1.7 ka (Fig. 10). A possible explanation for the multiple OSL ages of the loess deposits at the ruptures along the scarps is episodic faulting-induced rupture growth and subsequent loess sedimentation, as suggested by our model (Fig. 6). Therefore, the chronology data of the trapped loess along HTB1 suggests that the Hutubi Fault was active from the early to mid-Holocene, while the Manas Fault was active from the mid- to late Holocene. However, the different OSL ages of the loess at ruptures along the scarps can be also explained in other ways, e.g. colluvial re-deposition, disturbance of the loess after multiple rupture events or continuous (discontinuous) loess deposition after a single rupture event. Nevertheless, in any case, the ages of the terrace treads and the oldest loess preserved at ruptures along the fault scarps should constrain the maximum and minimum ages of the scarps studied, respectively.

6. Discussion

Slip rates of the Hutubi and Manas faults

Based on the topographic profiles measured across the investigated fault scarps and the chronology data, we calculated vertical slip rates for both reverse faults (Table 4). The Hutubi Fault has vertically displaced terrace T-5 by 4.2 ± 0.4 m (cross-section B-B′). As the oldest loess sample preserved in exposure HTB1 and age of the terrace tread of T-5 were constrained at 10.5 ±1.0 and 12.4 ± 0.8 ka (Gong et al., 2014), respectively, the maximum and minimum vertical slip rates of the Hutubi Fault within the Manas Anticline were calculated at 0.40 ± 0.05 and 0.34 ± 0.04 mm/yr, respectively, during the late

Quaternary. Similarly, the Hutubi Fault has vertically displaced terrace T-6 by 7.8 ± 0.8 m (cross-section C-C′) (Fig. 4(b)). The age of the tread of T-6 is 19.9 ± 1.5 ka (Gong et al., 2014), which constrains the maximum age of HTB0. The offset and age of the T-6 tread yields a minimum vertical slip rate of 0.39 ± 0.05 mm/yr (Table 3). The two sets of data from T-5 and T-6 suggest that the vertical slip rate of the Hutubi Fault within the Manas Anticline was at about 0.4 mm/yr during last ~ 12 ka.

T-5 was vertically displaced by 9.2 ± 0.9 m by the Manas Fault, as shown in cross-section D-D′ in Fig. 4(b). As the oldest loess sample preserved along exposures of MNS1-MNS4 and the age of terrace tread T-5 were constrained at 5.7 ± 0.6 and 12.4 ± 0.8 ka, respectively (Gong et al., 2014), the maximum and minimum vertical slip rates of the Manas Fault are 1.6 ± 0.2 mm/yr and 0.74 ± 0.09 mm/yr, respectively. If it is assumed that the loess was deposited and preserved at the surface ruptures soon after the faulting events, the vertical slip rate of the Manas Fault is close to 1.6 ± 0.2 mm/yr during the late Holocene. It is to be noted that the evaluation of the vertical slip rates of the two reverse faults also depends on the observation timescale. Due to the intermittency of faulting events along the Manas and Hutubi faults, measurements of fault slip rates over timescales shorter than the longest gap will overestimate long-term average fault slip rates. For instance, an earthquake in the near future with an offset of 1-2 m would increase the cumulative offset of 4.2 m (fault displacement of HTB1) to 5.2-6.2 m, with a similar rise in the slip rate. To better compare the faulting along the Manas and Hutubi faults, their vertical slip rates were compared over the same timescale: i.e. from the formation the tread of T-5 (~12.4 ka) to the present. It is found that the correspondingly vertical slip rates of the Manas and Hutubi faults are calculated at 0.74 ± 0.09 mm/yr and 0.34 ± 0.04 mm/yr, respectively. In addition, it is also interesting to calculate the horizontal shortening rate and the fault slip rate of the two reverse faults. Although the strata along the scarps were not fully revealed by our trenches, the dip angles of the two reverse faults at the surface can be estimated based on the results from previous studies (Avouac et al., 1993; Zhao et al., 2001). In this study, a dip angle of 45 ± 5° of the Manas Fault (Zhao et al., 2001) is used to calculate the slip rates of the Manas Fault. The horizontal shortening rate and the total slip rate of the Manas Fault are calculated at 0.74

± 0.17 mm/yr and 1.05 ± 0.16 mm/yr, respectively. For the Hutubi Fault, a dip angle of 55 ± 5° (Avouac et al., 1993) is used to calculate the slip rates, and the horizontal shortening rate and the total slip rate of the Hutubi Fault are calculated at 0.24 ± 0.06 mm/yr and 0.42 ± 0.06 mm/yr, respectively. The results show that the Manas Fault exhibits a higher slip rate than the Hutubi Fault at the site during the Holocene.

It is also interesting to note that the oldest OSL age of the loess trapped at the surface ruptures along the Manas Fault (MNS1-MNS4) is ~5.7 ka, while significantly older loess deposits were found at HTB1. One of the possible explanations is that the Manas Fault was relatively inactive during the early to mid-Holocene and the faulting at the studied area mainly occurred at the Hutubi Fault during that period. From the mid-Holocene to the present, tectonic deformation probably accelerated in the northern foreland basin, not only making the Manas Fault active, but also leading to more significantly surface rupturing events along the Manas Fault. In addition, the loess of ~4 ka was identified at the surface ruptures along both the Hutubi and Manas faults, indicating that both the Hutubi Fault and the Manas Fault were ruptured in a large, surface-rupturing earthquakes at ~ 4 ka. An alternative explanation for our results is that the Manas Fault was also active during the early to mid-Holocene, but the faulting events along the Manas Fault older than 6 ka were not recorded due to the lack of terrace preservation. Thus, to further examine whether there is accelerated tectonic deformation in the northern foreland basin of Tian Shan, more studies on different fault segments in the area should be carried out in the future, in order to obtain more data on the faulting at different timescale during the Quaternary.

7. Conclusions

In the northern foreland basin of Tian Shan, the fluvial terraces along the Manas River were ruptured by the Manas and Hutubi faults, forming fault scarps several meters in height. OSL dating results for the trapped loess preserved at the surface ruptures along the fault scarps show that the Hutubi Fault was active from the early to mid-Holocene, while the Manas Fault was active from the mid- to late Holocene. Together with

high-resolution differential global position system (GDPS) measurements on the fault scarps, the corresponding vertical slip rates of the Manas and Hutubi faults were calculated and compared. During the late Quaternary, the vertical slip rates of the Manas Fault are constrained to between ~0.74 mm/yr and ~1.6 mm/yr, whilst those of the Hutubi Fault are constrained to between ~0.34 mm/yr and ~0.40 mm/yr in the studied region. The tectonic uplift activity in the northern foreland basin of Tian Shan likely accelerated during the late Quaternary.

Acknowledgements

The authors would like to thank Anchuan Fan, Zhengqing Zhang and Junliang Ji for their help during fieldwork, Jimin Sun, Bihong Fu, Huiping Zhang and Zhonghua Tian for improving our manuscript, and Michael Pittman for English editing. This study was financially supported by grants awarded to Sheng-Hua Li from the Research Grant Council of the Hong Kong Special Administrative Region, China (Project no. 7028/08P and 7033/12P). The authors thank An Yin and two anonymous reviewers for providing valuable comments and suggestions on the manuscript.

References

Abdrakhmatov, K.Y., Aldazhanov, S.A., Hager, B.H., Hamburger, M.W., Herring, T.A., Kalabaev, K.B., Makarov, V.I., Molnar, P., Panasyuk, S.V., Prilepin, M.T., Reilinger, R.E., Sadybakasov, I.S., Souter, B.J., Trapeznikov, Y.A., Tsurkov, V.Y., Zubovich, A.V., 1996. Relatively recent construction of the Tien Shan inferred from GPS measurements of present-day crustal deformation rates. Nature 384, 450-453.

Aitken, M.J., 1998. An Introduction to Optical Dating. Oxford Unversity Press, Oxford.

Avouac, J.P., Tapponnier, P., Bai, M., You, H. Wang, G., 1993. Active Thrusting and Folding along the Northern Tian Shan and Late Cenozoic Rotation of the Tarim Relative to Dzhugaria and Kazakhstan. Journal of Geophysical Research 98, 6755-6804.

Bøtter-Jensen, L., Andersen, C.E., Duller, G.A.T., Murray, A.S., 2003. Developments in radiation, stimulation and observation facilities in luminescence measurements. Radiation Measurements 37, 535-541.

Burchfiel, B.C., Brown, E.T., Deng, Q.D., Feng, X.Y., Li, J., Molnar, P., Shi, J.B., Wu, Z.M., You, H.C., 1999. Crustal shortening on the margins of the Tien Shan, Xinjiang, China. International Geology Review 41, 665-700.

Charreau, J., Chen, Y., Gilder, S., Barrier, L., Dominguez, S., Augier, R., Sen, S., Avouac, J.-P., Gallaud, A., Graveleau, F., and Wang, Q., 2009, Neogene uplift of the Tian Shan Mountains observed in the magnetic record of the Jingou River section (northwest China): Tectonics 28, TC2008, doi: 10.1029/2007TC002137.

Charreau, J., Chen, Y., Gilder, S., Dominguez, S., Avouac, J.-P., Sen, S., Sun, D., Li, Y., and Wang, W.-M., 2005, Magnetostratigraphy and rock magnetism of the Neogene Kuitun He section (northwest China): implications for Late Cenozoic uplift of the Tianshan mountains: Earth and Planetary Science Letters 230, 177-192.

Chen, Y.-G., Chen, Y.-W., Chen, W.-S., Lee, K.-J., Lee, L.-S., Lu, S.-T., Lee, Y.-H., Watanuki, T., Lin, Y.-N.N., 2009. Optical dating of a sedimentary sequence in a trenching site on the source fault of the 1999 Chi-Chi earthquake, Taiwan.

Quaternary International 199, 25-33.

Chen, Y., Li, S.-H. and Li, B., 2012. Slip rate of the Aksay segment of Altyn Tagh Fault revealed by OSL dating of river terraces. Quaternary Geochronology, 10(0): 291-299.

Chen, Y., Li, S.-H., Sun, J. and Fu, B., 2013. OSL dating of offset streams across the Altyn Tagh Fault: Channel deflection, loess deposition and implication for the slip rate. Tectonophysics, 594(0): 182-194.

Cheong, C.S., Hong, D.G., Lee, K.S., Kim, J.W., Choi, J.H., Murray, A.S., Chwae, U., Im, C.B., Chang, C.J., Chang, H.W., 2003. Determination of slip rate by optical dating of fluvial deposits from the Wangsan fault, SE Korea. Quaternary Science Reviews 22, 1207-1211.

Deng, Q.D., Zhang, P.Z., Xu, X.W., Yang, X.P., Peng, S.Z., Feng, X.Y., 1996. Paleoseismology of the northern piedmont of Tianshan Mountains, northwestern China. Jounal of Geophysical Research-Solid Earth 101, 5895-5920.

Fang, X.M., Shi, Z.T., Yang, S.L., Yan, M.D., Li, J.J., and Jiang, P.A., 2002, Loess in the Tian Shan and its implications for the development of the Gurbantunggut Desert and drying of northern Xinjiang. Chinese Science Bulletin 47, 1381-1387.

Forman, S.L., Nelson, A.R., Mccalpin, J.P., 1991. Thermoluminescence Dating of Fault-Scarp-Derived Colluvium - Deciphering the Timing of Paleoearthquakes on the Weber Segment of the Wasatch Fault Zone, North Central Utah. Jounal of Geophysical Research-Solid Earth 96, 595-605.

Fu, B.H., Lin, A.M., Kano, K., Maruyama, T., Guo, J.M., 2003. Quaternary folding of the eastern Tian Shan, northwest China. Tectonophysics 369, 79-101.

Fu, B., Walker, R., and Sandiford, M., 2011, The 2008 Wenchuan earthquake and active tectonics of Asia: Journal of Asian Earth Sciences 40, 797-804.

Fu, X., Li, B., Li, S.-H., 2012. Testing a multi-step post-IR IRSL dating method using polymineral fine grains from Chinese loess. Quaternary Geochronology 10, 8-15.

Kahle, J. E., 1975. Surface effects and related geology of the Lakeview fault segment of the San Fernando fault zone. California Division of Mines and Geology Bulletin 196, 119–135.

Küster, Y., Hetzel, R., Krbetschek, M., and Tao, M., 2006, Holocene loess sedimentation along the Qilian Shan (China): significance for understanding the processes and timing of loess deposition. Quaternary Science Reviews 25, 114-125.

Galbraith, R.F., Roberts, R.G., Laslett, G.M., Yoshida, H., Olley, J.M., 1999. Optical dating of single and multiple grains of quartz from Jinmium rock shelter, northern Australia, part 1, Experimental design and statistical models. Archaeometry 41, 339-364.

Gong, Z., Li, S.-H., Sun, J., and Xue, L., 2013, Environmental changes in Hunshandake (Otindag) sandy land revealed by optical dating and multi-proxy study of dune sands: Journal of Asian Earth Sciences 76, 30-36.

Gong, Z.J., Li, S,-H., Li, B., 2014. The evolution of a terrace sequence along Manas River in the northern piedmont of TianShan, China, as inferred from optical dating. Geomorphology 213, 201-212.

Heermance, R.V., Chen, J., Burbank, D.W., and Wang, C., 2007, Chronology and tectonic controls of Late Tertiary deposition in the southwestern Tian Shan foreland, NW China: Basin Research 19, 599-632.

Jacobs, Z., Duller, G.A.T., Wintle, A.G., 2003. Optical dating of dune sand from Blombos Cave, South Africa: II - single grain data. Journal of Human Evolution 44, 613-625.

Li, B., Li, S.-H., 2011. Luminescence dating of K-feldspar from sediments: A protocol without anomalous fading correction. Quaternary Geochronology 6, 468-479.

Li, B., Roberts, R.G., Jacobs, Z., and Li, S.-H., 2014, A single-aliquot luminescence dating procedure for K-feldspar based on the dose-dependent MET-pIRIR signal sensitivity. Quaternary Geochronology 20, 51-64.

Li, S.-H., Chen, Y.Y., Li, B., Sun, J.M., Yang, L.R., 2007. OSL dating of sediments from deserts in northern China. Quaternary Geochronology 2, 23-28.

Li, S.-H., Fan, A.C., 2011. OSL chronology of sand deposits and climate change of last 18 ka in Gurbantunggut Desert, northwest China. Journal of Quaternary Science 26, 813-818.

Li, S.-H., Sun, J.M., Li, B., 2012. Holocene environmental changes in central Inner

Mongolia revealed by luminescence dating of sediments from the Sala Us River valley. Holocene 22, 397-404.

Li, S.-H., Sun, J.M., Zhao, H., 2002. Optical dating of dune sands in the northeastern deserts of China. Palaeogeography, Palaeoclimatology, Palaeoecology 181, 419-429.

Lu, H.H., Burbank, D.W., Li, Y.L., Liu, Y.M., 2010. Late Cenozoic structural and stratigraphic evolution of the northern Chinese Tian Shan foreland. Basin Research 22, 249-269.

Molnar, P., Tapponnier, P., 1975. Cenozoic Tectonics of Asia - Effects of a Continental Collision. Science 189, 419-426.

Murray, A.S., Wintle, A.G., 2000. Luminescence dating of quartz using an improved single-aliquot regenerative-dose protocol. Radiation Measurements 32, 57-73.

Nogueira, F.C., Bezerra, F.H.R., Fuck, R.A., 2010. Quaternary fault kinematics and chronology in intraplate northeastern Brazil. Journal of Geodynamics 49, 79-91.

Olley, J.M., Caitcheon, G.G., Roberts, R.G., 1999. The origin of dose distributions in fluvial sediments, and the prospect of dating single grains from fluvial deposits using optically stimulated luminescence. Radiation Measurements 30, 207-217.

Poisson, B., and Avouac, J.P., 2004, Holocene Hydrological Changes Inferred from Alluvial Stream Entrenchment in North Tian Shan (Northwestern China). The Journal of Geology 112, 231 - 249.

Prescott, J.R., Hutton, J.T., 1994. Cosmic-Ray Contributions to Dose-Rates for Luminescence and Esr Dating - Large Depths and Long-Term Time Variations. Radiation Measurements 23, 497-500.

Rhodes, E.J., 2011, Optically Stimulated Luminescence Dating of Sediments over the Past 200,000 Years. Annual Review of Earth and Planetary Sciences 39, 461-488.

Stokes, S., Hetzel, R., Bailey, R.M., and Mingxin, T., 2003, Combined IRSL-OSL single aliquot regeneration (SAR) equivalent dose (De) estimates from source proximal Chinese loess. Quaternary Science Reviews 22, 975-983.

Sun, J., 2002, Source Regions and Formation of the Loess Sediments on the High

561 Mountain Regions of Northwestern China. Quaternary Research 58, 341-351.
562 Sun, J. M., Li, S.-H., Han, P., Chen, Y. Y., 2006. Holocene environmental changes in the
563 central Inner Mongolia, based on single-aliquot-quartz optical dating and
564 multi-proxy study of dune sands. Palaeogeography, Palaeoclimatology,
565 Palaeoecology 233, 51-62.
566 Sun, J.M., Zhang, Z.Q., 2009. Syntectonic growth strata and implications for late
567 Cenozoic tectonic uplift in the northern Tian Shan, China. Tectonophysics 463,
568 60-68.
569 Tapponnier, P., Molnar, P., 1979. Active Faulting and Cenozoic Tectonics of the Tien
570 Shan, Mongolia, and Baykal Regions. Journal of Geophysical Research 84,
571 3425-3459.
572 Wang, X.L., Wintle, A.G., and Lu, Y.C., 2006, Thermally transferred luminescence in
573 fine-grained quartz from Chinese loess: Basic observations. Radiation
574 Measurements 41, 649-658.
575 Xu, X.W., Deng, Q.D., Zhang, P.Z., Feng, X.Y., Li, J., Wu, Z.M., Yang, X.P., Zhao, R.B.,
576 Tang, W., 1992. Deformation of River Terraces Across the Manas-Huoerguous
577 Reverse Fault and Fold Zone and Its Neotiectonic Implication in Xinjiang (in
578 Chinese). Research on active fault 2, 117-127.
579 Zhang, P.Z., 2004. Late Cenozoic tectonic deformation in the Tianshan Mountain and its
580 foreland basins. Chinese Science Bulletin 49, 311-313.
581 Zhang, J.F., Qiu, W.L., Li, R.Q., Zhou, L.P., 2009. The evolution of a terrace sequence
582 along the Yellow River (HuangHe) in Hequ, Shanxi, China, as inferred from
583 optical dating. Geomorphology 109, 54-65.
584 Zhao, C.-B., Sun, Z.-G., Gu, M.-L., and Yang, X.-P., 2001, Prospecting and Study of
585 Shallow Crustal Structure in Manas Earthquake Area: Chinese Journal of
586 Geophysics 44, 48-58.
587
588
589
590

Table 1: the abandonment ages of the six terraces along the Manas River in the study area. For the detail of the ages of the terraces, please refer to Gong et al. (2014).

Terraces	T-1	T-2	T-3	T-4	T-5	T-6
Optical ages, ka	0.5±0.1	1.4±0.3	3.1±0.3	4.0±0.4	12.4±0.8	19.9±1.5

Table 2: the dose rate results for loess samples from the five exposures of the fault scarps (HTB1, MNS1-MNS4) in the study area.

Sample	depth (m)	Alpha counting rate[a]	K content(%)	Water content[b] (%)	Cosmic ray[c] (Gy/ka)	Dose rate (Gy/ka)
HububiFault						
HTB1-1	0.3	10.9±0.2	2.27±0.23	6.0	0.23	3.85±0.16
HTB1-2	0.4	9.53±0.19	1.86±0.19	4.6	0.22	3.32±0.16
HTB1-3	0.5	10.7±0.21	2.10±0.21	3.2	0.22	3.77±0.16
HTB1-4	1.2	11.5±0.21	2.09±0.21	3.3	0.20	3.85±0.16
HTB1-5	0.8	10.9±0.21	2.30±0.23	2.0	0.21	3.86±0.16
HTB1-6	1.6	10.8±0.21	2.10±0.21	6.7	0.19	3.63±0.16
HTB1-7	1.0	10.7±0.20	2.20±0.22	8.7	0.21	3.60±0.16
ManasFault						
MNS1						
MNS1-1	0.3	10.5±0.21	1.86±0.19	5.6	0.22	3.39±0.14
MNS1-2	0.7	10.4±0.20	2.01±0.20	7.6	0.21	3.42±0.15
MNS1-3	0.5	10.1±0.20	2.00±0.20	7.1	0.22	3.40±0.15
MNS1-4	0.5	10.6±0.21	2.00±0.20	8.8	0.22	3.40±0.16
MNS1-5	1.0	10.4±0.21	2.12±0.21	9.6	0.20	3.48±0.16
MNS1-6	1.0	9.55±0.19	2.20±0.22	8.7	0.20	3.47±0.16
MNS1-7	0.8	9.34±0.19	2.05±0.21	8.5	0.21	3.32±0.16
MNS2						
MNS2-1	0.5	10.2±0.2	2.30±0.23	3.4	0.22	3.82±0.17
MNS2-2	1.0	10.1±0.2	2.18±0.22	3.0	0.20	3.70±0.16
MNS2-3	1.6	11.0±0.2	2.14±0.21	6.3	0.19	3.64±0.16
MNS2-4	2.0	11.1±0.2	2.21±0.22	9.2	0.18	3.59±0.16
MNS3						
MNS3-1	0.5	10.7±0.2	2.18±0.22	3.7	0.22	3.83±0.17
MNS3-2	0.5	10.3±0.2	2.17±0.22	2.0	0.22	3.82±0.17
MNS3-3	1.0	11.0±0.2	2.39±0.24	2.1	0.20	4.11±0.19
MNS3-4	1.0	9.77±0.22	1.93±0.19	1.0	0.20	3.54±0.15
MNS3-5	1.0	10.5±0.2	2.31±0.23	1.0	0.20	4.01±0.18
MNS4						
MNS4-1	0.5	9.57±0.20	2.13±0.21	10.2	0.22	3.38±0.16
MNS4-2	0.8	9.56±0.20	2.11±0.21	11.0	0.21	3.32±0.16
MNS4-3	1.0	10.1±0.2	2.24±0.22	7.7	0.20	3.62±0.17
MNS4-4	0.5	10.6±0.2	2.20±0.22	10.1	0.22	3.58±0.17
MNS4-5	1.0	9.71±0.20	2.30±0.23	8.4	0.20	3.59±0.17

[a]The alpha counting rate is for a 42-mm-diameter ZnS screen and is given in units of counts per kilo second.

[b] The error for the water content is estimated at ±20 %.

623[c] The error for the cosmic rays dose rate is estimated at ± 0.02 Gy/ka.

624 Table 3: quartz OSL ages for the loess samples from the five exposures of the fault scarps

625 (HTB1, MNS1-MNS4) in the study area.

626

Sample	aliquots	Over-dispersion values (%)	Mean Age model De (Gy)	Mean Age model Age (ka)	Central Age model D_e (Gy)	Central Age model Age (ka)
HububiFault						
HTB1-1	20	26.5±2.2	16.2±1.4	4.2±0.4	15.7±1.4	4.1±0.4
HTB1-2	20	28.5±1.7	29.1±2.7	8.8±0.9	27.5±2.7	8.3±0.9
HTB1-3	26	39.3±1.2	32.5±3.4	8.6±1.0	30.0±2.4	7.9±0.7
HTB1-4	20	31.5±1.4	40.3±3.6	10.5±1.0	38.4±3.0	10.0±0.9
HTB1-5	20	29.8±1.1	16.1±1.2	4.2±0.3	15.4±1.1	4.0±0.3
HTB1-6	20	24.2±0.9	23.3±1.4	6.4±0.5	22.6±1.2	6.2±0.4
HTB1-7	20	20.5±0.9	15.3±1.2	4.3±0.4	15.5±0.8	4.3±0.3
ManasFault						
MNS1						
MNS1-1	20	33.5±2.3	8.1±1.7	2.4±0.5	6.8±1.1	2.0±0.3
MNS1-2	20	30.5±1.4	19.4±1.8	5.7±0.6	18.9±1.5	5.5±0.5
MNS1-3	20	27.6±1.6	8.1±0.7	2.4±0.2	7.9±0.6	2.3±0.2
MNS1-4	20	30.0±1.4	10.4±0.8	3.1±0.3	10.3±0.8	3.0±0.3
MNS1-5	20	24.2±0.9	14.5±0.8	4.2±0.3	14.1±0.8	4.0±0.3
MNS1-6	20	34.8±1.6	17.8±1.7	5.1±0.5	16.6±1.5	4.8±0.5
MNS1-7	20	24.2±1.9	13.7±1.1	4.1±0.4	13.3±1.1	4.0±0.4
MNS2						
MNS2-1	20	22.1±1.6	6.5±0.5	1.7±0.1	7.1±0.5	1.9±0.2
MNS2-2	20	16.8±1.0	9.5±0.6	2.6±0.2	9.6±0.4	2.6±0.2
MNS2-3	20	32.9±1.6	11.3±0.9	3.1±0.3	10.5±1.0	2.9±0.3
MNS2-4	20	27.6±1.3	11.9±0.8	3.3±0.3	11.4±0.8	3.2±0.3
MNS3						
MNS3-1	20	34.1±1.7	15.4±1.5	4.0±0.4	14.1±1.5	3.7±0.4
MNS3-2	20	39.8±1.6	15.4±1.9	4.0±0.5	14.4±1.4	3.8±0.4
MNS3-3	20	13.3±0.7	14.0±0.4	3.4±0.2	14.1±0.5	3.4±0.2
MNS3-4	20	33.6±1.6	19.2±1.7	5.4±0.5	17.9±1.6	5.1±0.5
MNS3-5	21	25.8±1.0	19.1±1.3	4.7±0.4	18.4±1.1	4.6±0.3
MNS4						
MNS4-1	20	35.0±1.5	7.7±0.8	2.3±0.3	7.3±0.6	2.2±0.2
MNS4-2	20	39.5±1.5	14.0±1.4	4.2±0.5	13.0±1.2	3.9±0.4
MNS4-3	20	26.4±1.1	15.7±1.1	4.3±0.4	15.1±1.0	4.2±0.3
MNS4-4	20	27.6±1.1	7.5±0.6	2.1±0.2	7.4±0.5	2.1±0.2
MNS4-5	20	34.0±1.4	19.1±1.9	5.3±0.6	18.1±1.5	5.0±0.5

627

Table 4: Estimations of the late Quaternary vertical slip rates of the Hutubi and Manas faults in the northern piedmont of Tian Shan.

	Deformed terrace	Cumulative vertical offset (m)	The onset time of deformation (ka)		Vertical slip rate (mm/yr)	
Hutubi Fault	T-5	4.2±0.4	minimum	maximum	minimum	maximum
			10.5 ± 1.0	12.4 ± 0.8	0.34 ± 0.04	0.40 ± 0.05
	T-6	7.8±0.8		20 ± 1.5	0.39 ± 0.05	
Manas Fault	T-5	9.2 ±0.9	5.7± 0.6	12.4 ± 0.8	0.74 ± 0.09	1.6 ± 0.2

637 **Figure captions**

638

639 Figure 1(a): A color-shaded relief map with a simplified active tectonic map of Asia and
640 surrounding regions (modified from Fu et al. (2011)). (b): Interpretative geologic map of
641 three roughly east-west stretching fold and fault zones along the northern piedmont of
642 Tian Shan (modified from Sun et al. (2009)). The dip of the Hutubi and Manas faults at
643 the surface were from Avouac et al. (1993) and Zhao et al. (2001), respectively.

644

645 Figure 2(a): Landsat TM image showing the deformational features of the Manas and
646 Hutubi faults in the northern piedmont of Tian Shan. (b): Schematic geomorphology of
647 Manas River terraces within the Manas Anticline area. The terraces (T-5 and T-6) were
648 deformed intensively by the Hutubi and Manas faults, forming fresh-looking fault
649 scarps..

650

651 Figure 3: Conceptual graph showing the transportation and deposition of aeolian dust
652 from the Junggar Desert to the northern piedmont of Tian Shan (modified from Sun
653 (2002)).

654

655 Figure 4 (a): Google Earth map showing the studied sites and the locations of the fault
656 scarps. (b): A schematic graph showing the geomorphology of the T-5 and T-6 of the
657 Manas River. Six exposures (HTB0, HTB1, MNS1-MNS4) were studied to decipher late
658 Quaternary faulting along the Hutubi and Manas faults. The cumulative vertical
659 displacements of the reverse faults were measured from B-B′, C-C′ and D-D′. (c): A
660 schematic graph showing the relation among the surface ruptures, fault scarp and terrace
661 tread.

662

663 Figure 5: The exposures of the ruptures along the fault scarps and detailed OSL dating
664 sampling positions and (a) (HTB0) (we could not find any appropriate loess samples for
665 OSL dating, as the original fault scarp was destroyed as a result of the development of a
666 gully along the fault); (b) (HTB1); (c) (MNS1); (d) (MNS2); (e) (MNS3); (f) (MNS4).

667

668 Figure 6: Schematic diagrams showing the loess infilling at the surface ruptures along the
669 reverse fault scarps, in response to past faulting events. The process is illustrated with six
670 representative stages.

671

672 Figure 7: Single-aliquot regeneration (SAR) equivalent dose versus pre-heat temperature
673 for MNS2-4. The mean values with the standard errors are obtained from results of six
674 aliquots. The horizontal line denotes the pre-heat plateau was reached from 220 °C to
675 260 °C.

676

677 Figure 8: Typical OSL shine-down curves and OSL growth curves of quartz grains from
678 four loess samples (HTB1-4, MNS1-5, MNS2-1 and MNS3-4).

679

680 Figure 9: Radial plot results for D_e distributions of six loess samples from the five
681 exposures (HTB1, MNS1-MNS4). In the plot, the D_e and the OSL ages of the six
682 samples were calculated with the mean age model.

683

684 Figure 10: OSL dating results of the loess samples from the five exposures (HTB1,
685 MNS1-MNS4) along the scarps of the Hutubi and Manas faults.

686

Figure 1(a)

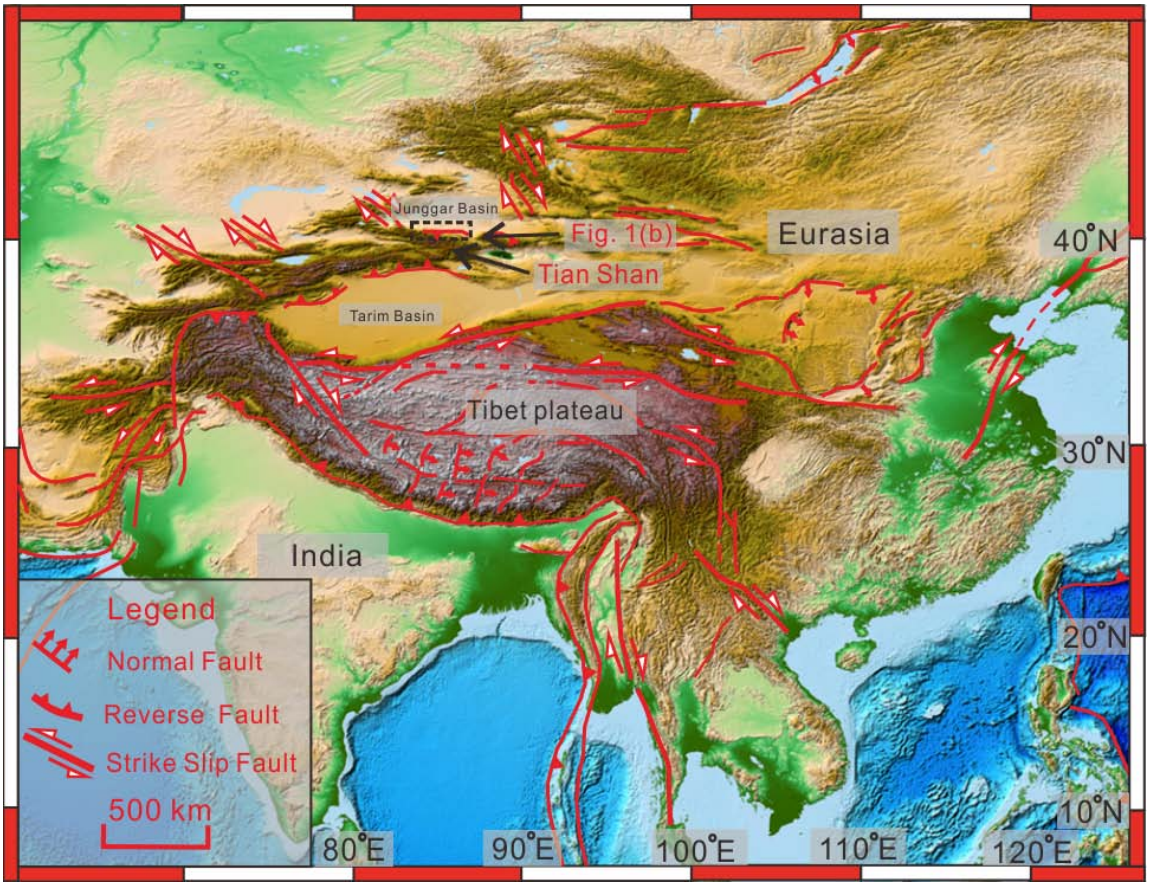

Figure 1(b)

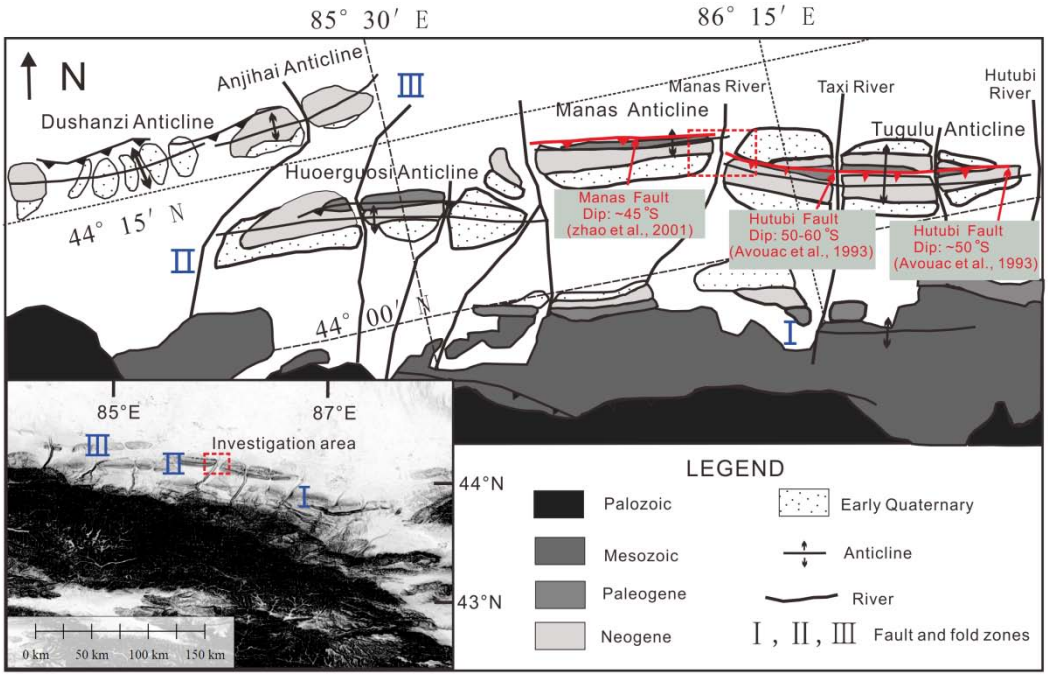

Figure 2(a)

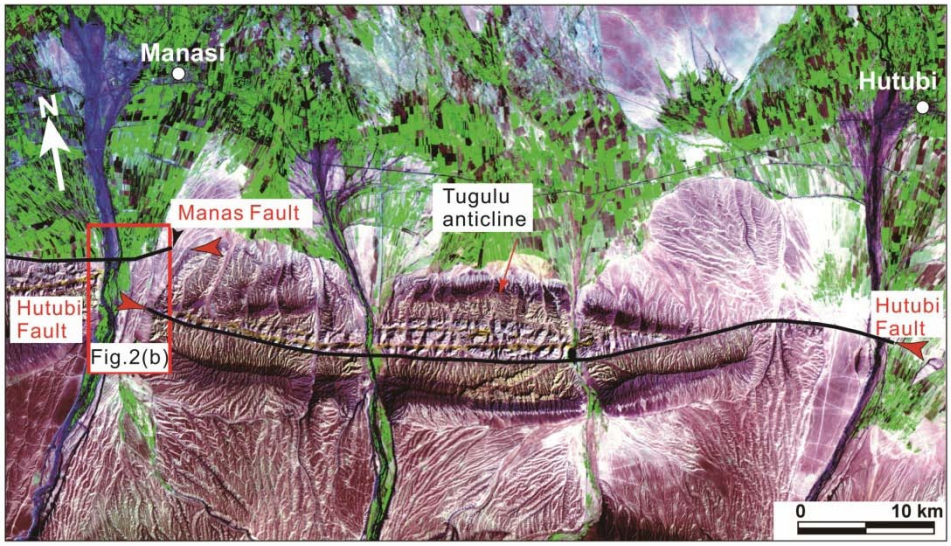

Figure 2(b)

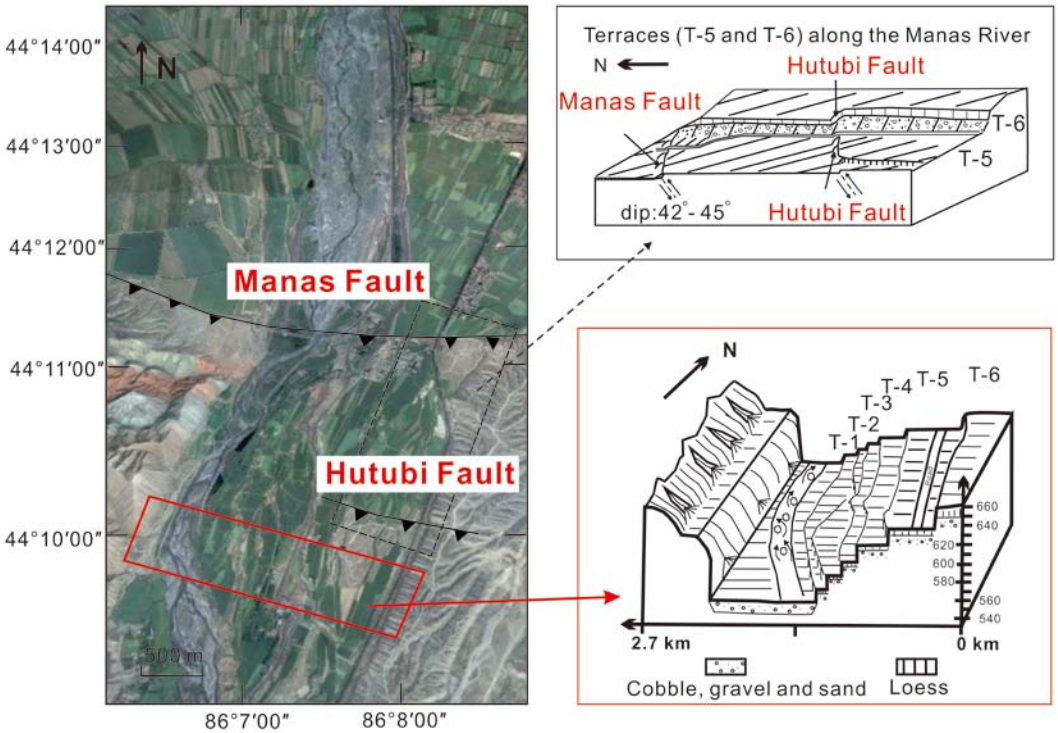

Figure 3

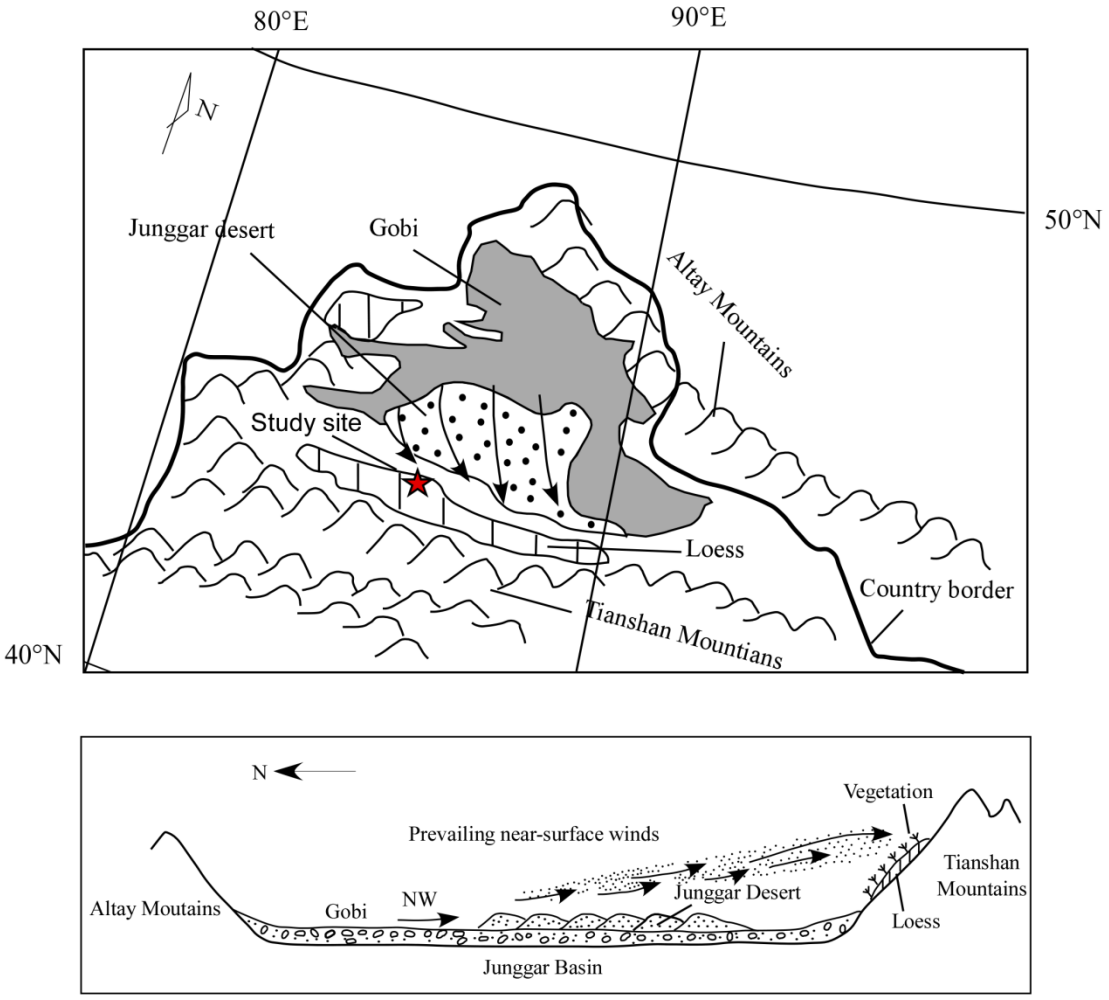
80°E
90°E
N
50°N
Junggar desert
Gobi
Altay Mountains
Study site
Loess
Country border
Tianshan Mountians
40°N
N
Vegetation
Prevailing near-surface winds
Tianshan
Mountains
Junggar Desert
Altay Moutains
Gobi
NW
Loess
Junggar Basin

Figure 4(a)

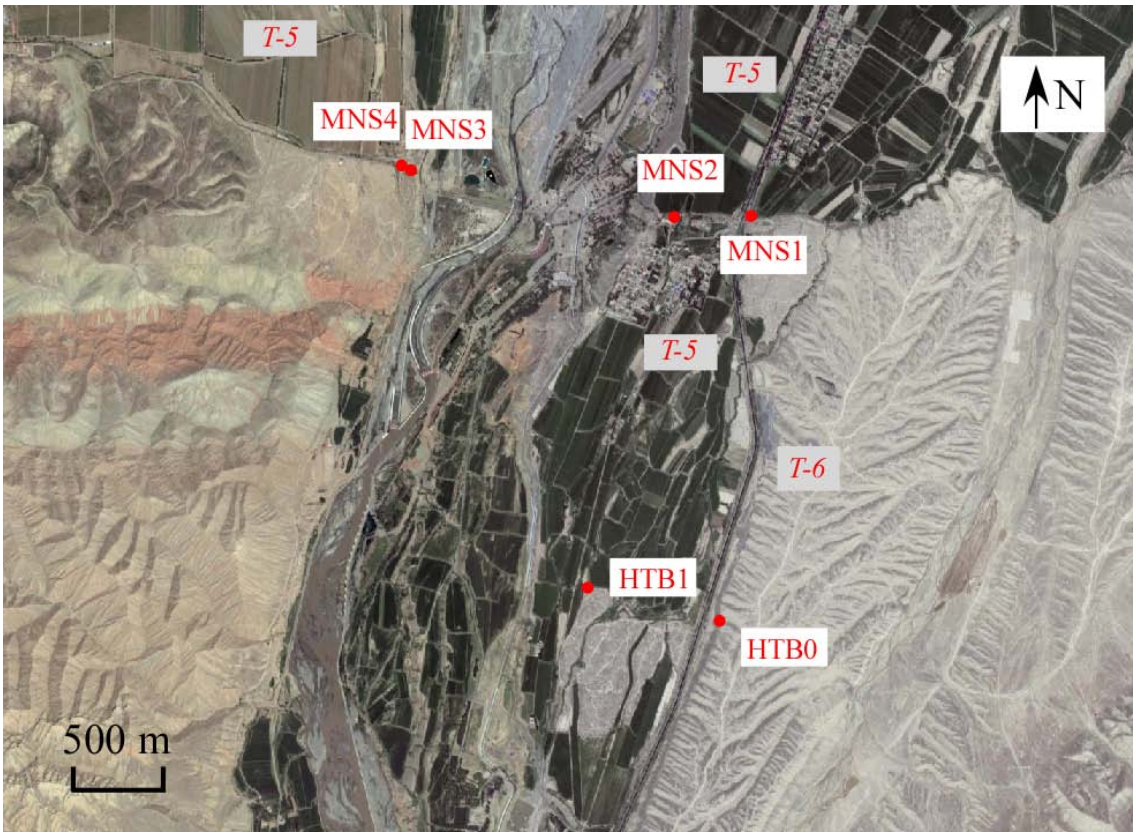

Figure 4(b)

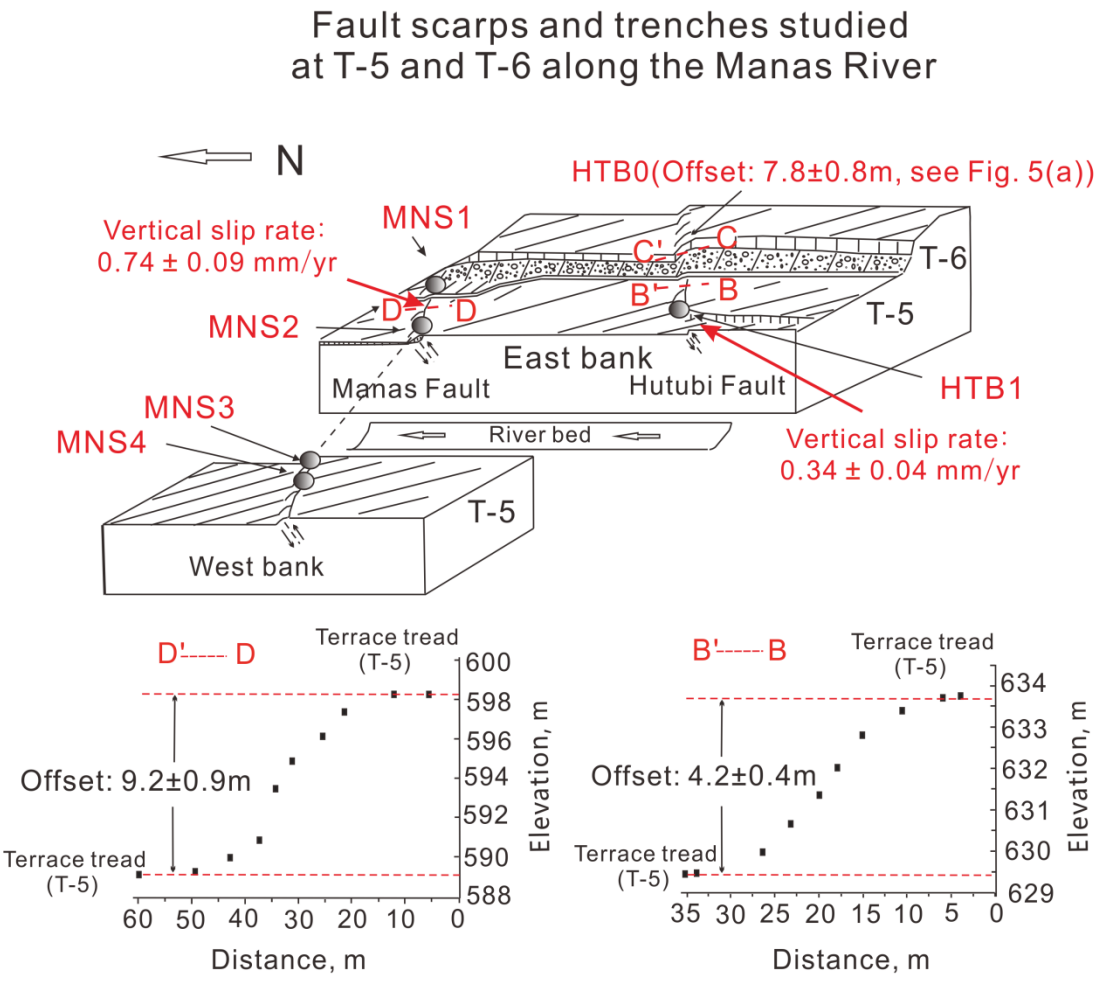
Fault scarps and trenches studied
at T-5 and T-6 along the Manas River
N
HTB0(Offset: 7.8±0.8m, see Fig. 5(a))
Vertical slip rate:
0.74 ± 0.09 mm/yr
MNS1
C'
C
T-6
B'
B
T-5
D'
D
MNS2
East bank
Manas Fault
Hutubi Fault
HTB1
MNS3
MNS4
River bed
Vertical slip rate:
0.34 ± 0.04 mm/yr
T-5
West bank
D'
D
Terrace tread
(T-5)
Offset: 9.2±0.9m
Terrace tread
(T-5)
600
598
596
594
592
590
588
Elevation, m
60 50 40 30 20 10 0
Distance, m
B'
B
Terrace tread
(T-5)
Offset: 4.2±0.4m
Terrace tread
(T-5)
634
633
632
631
630
629
Elevation, m
35 30 25 20 15 10 5 0
Distance, m

Fig. 4(c)

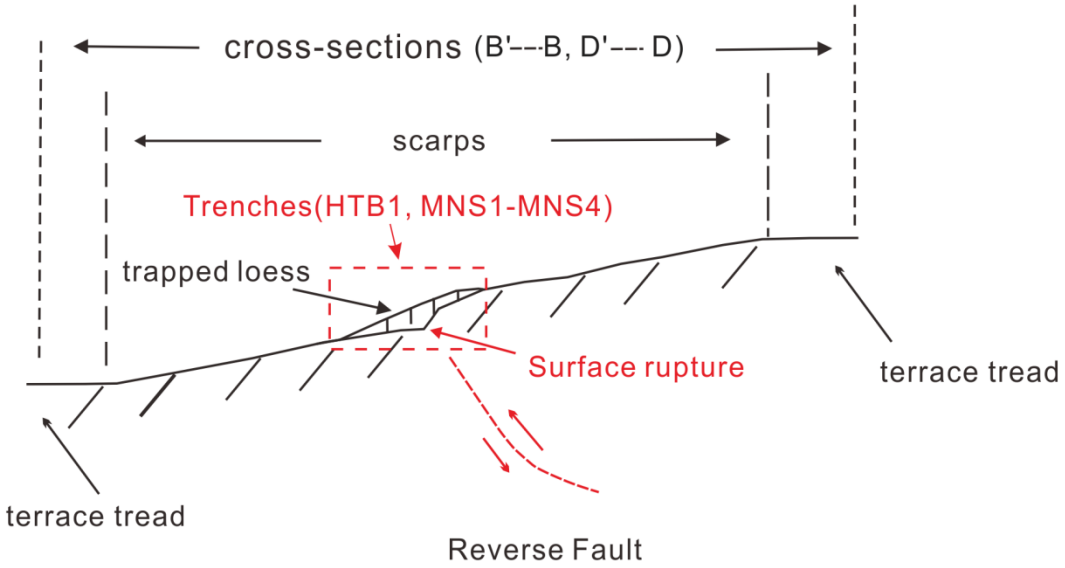
cross-sections (B'---B, D'---D)
scarps
Trenches(HTB1, MNS1-MNS4)
trapped loess
Surface rupture
terrace tread
terrace tread
Reverse Fault

Figure 5(a)

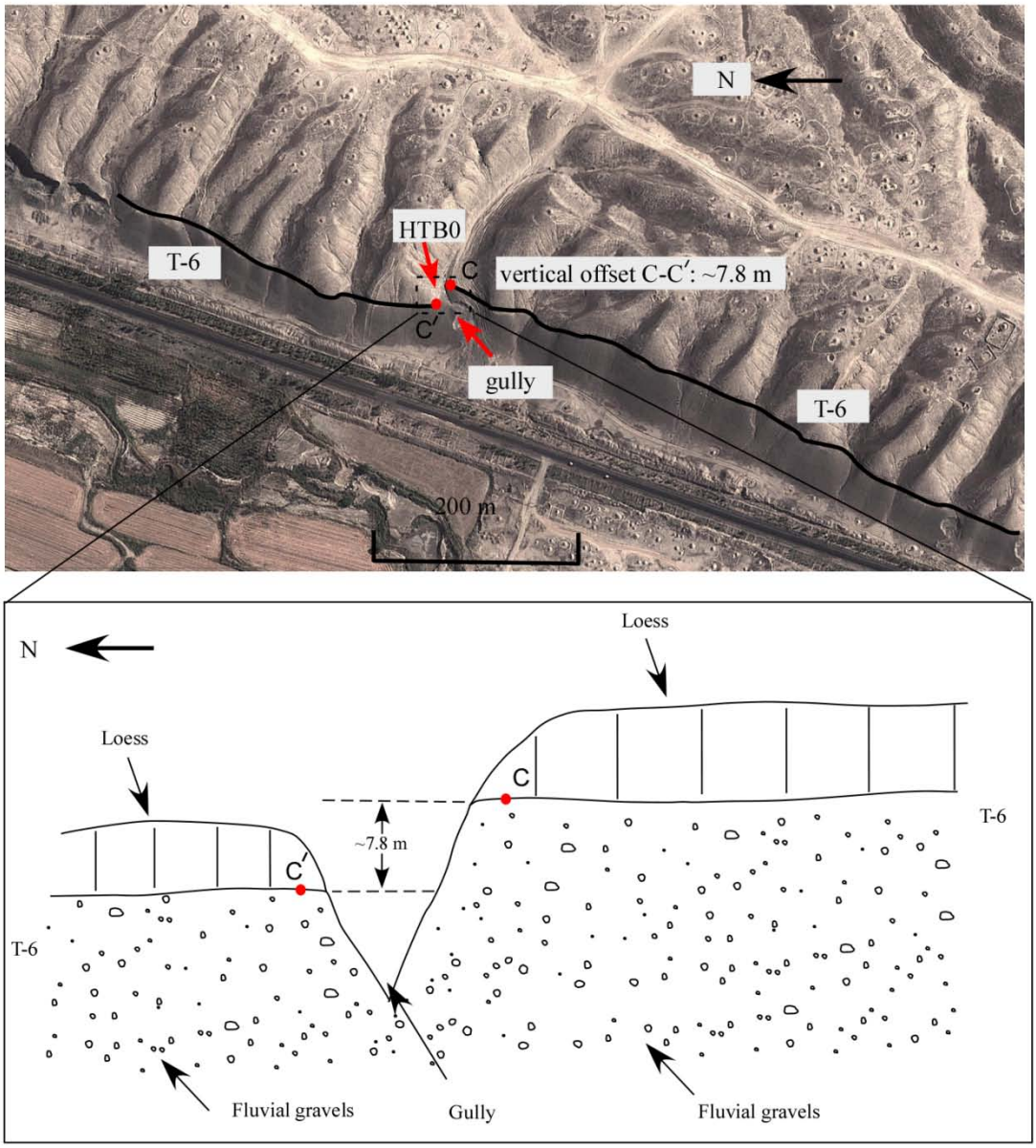
N
HTB0
T-6
C
vertical offset C-C′: ~7.8 m
C′
gully
T-6
200 m
N
Loess
Loess
C
T-6
~7.8 m
C′
T-6
Fluvial gravels
Gully
Fluvial gravels

Figure 5(b)

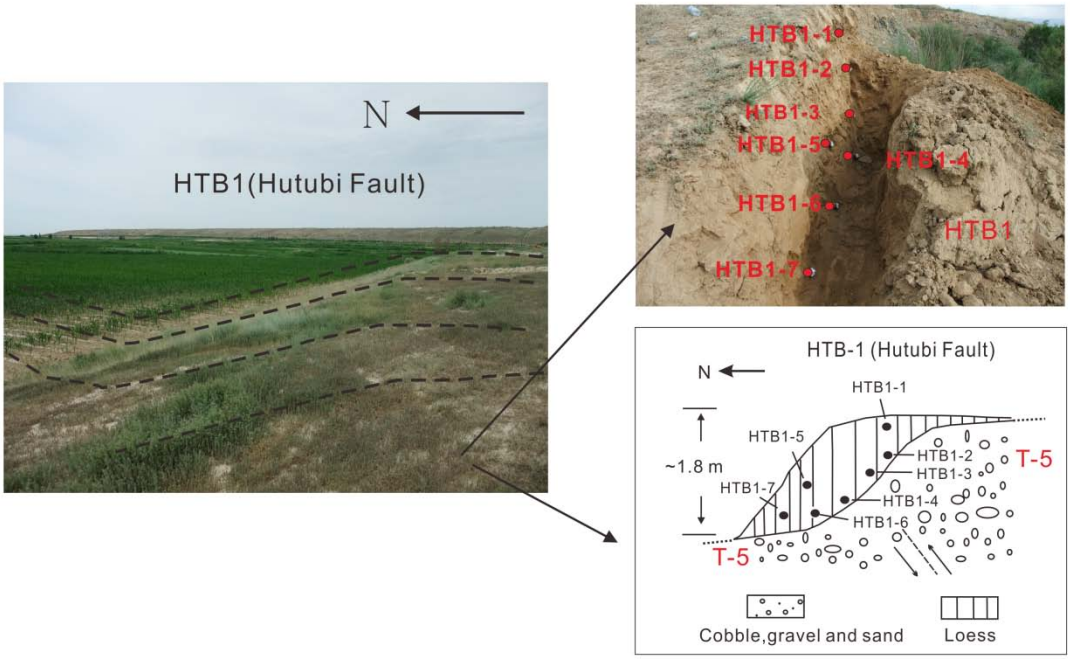

Figure 5(c)

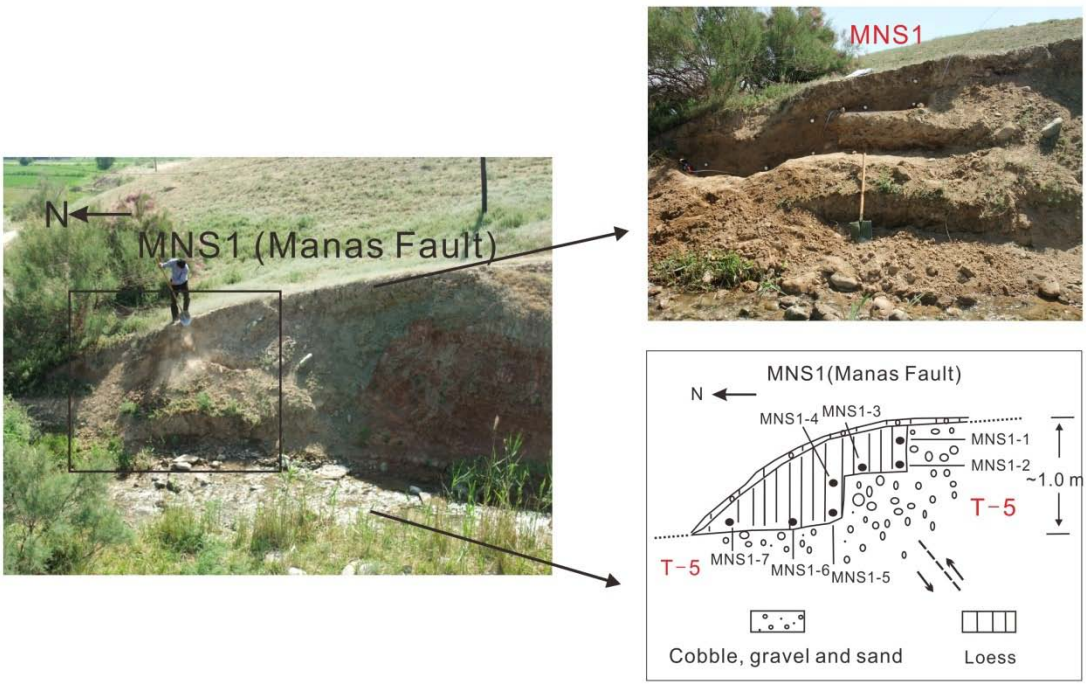

Figure 5(d)

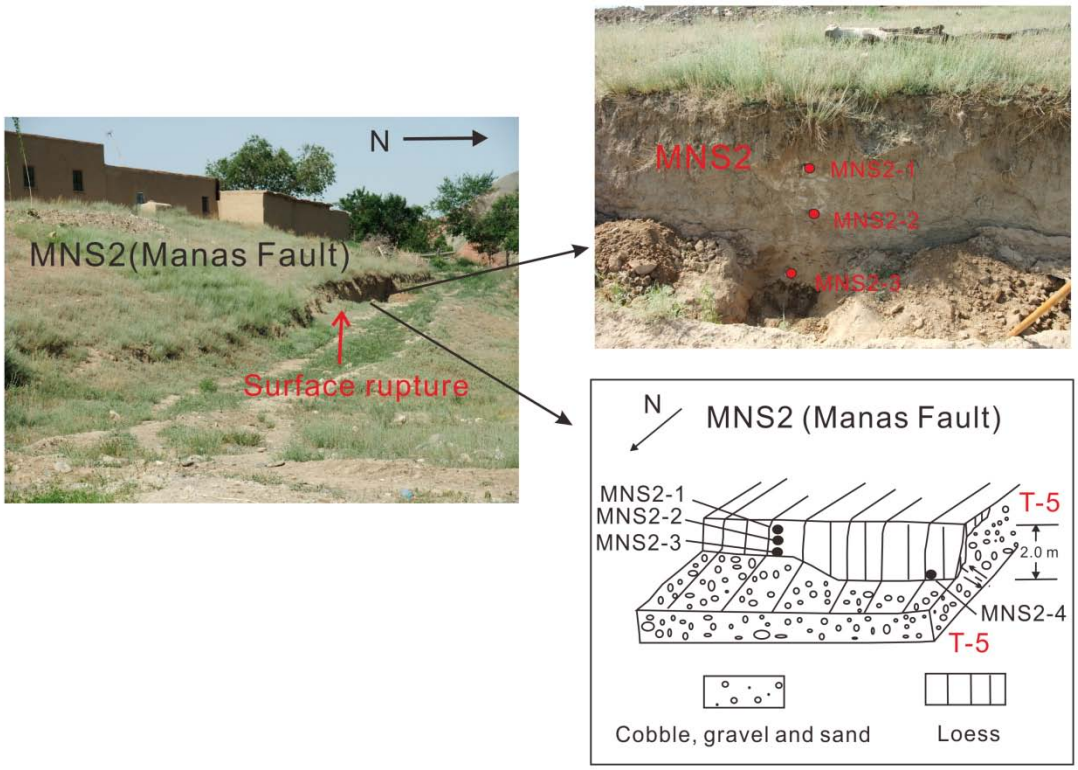

Figure 5(e)

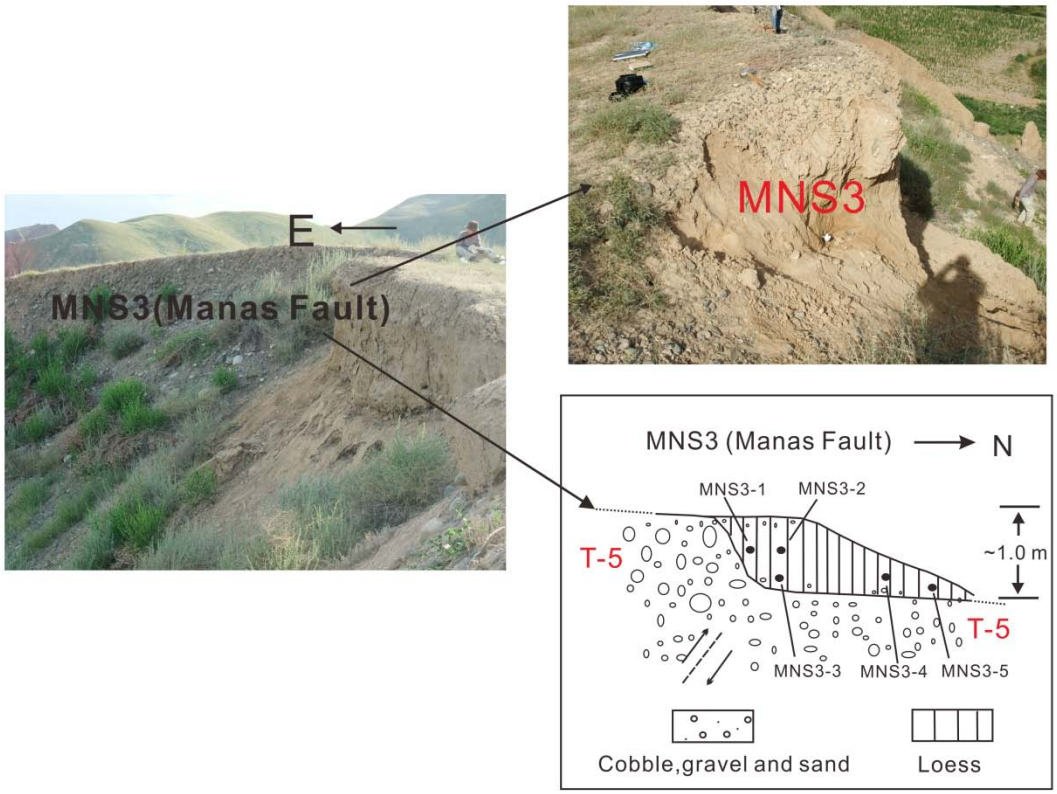

Figure 5(f)

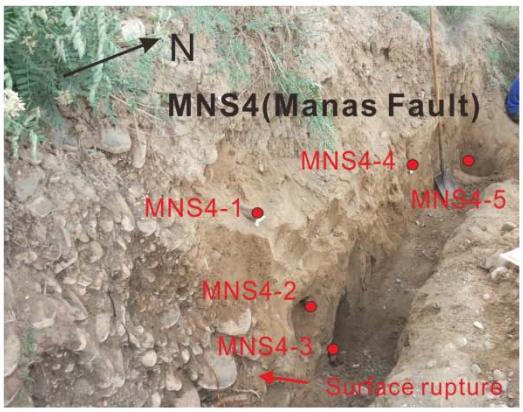
N
MNS4(Manas Fault)
MNS4-4
MNS4-5
MNS4-1
MNS4-2
MNS4-3
Surface rupture

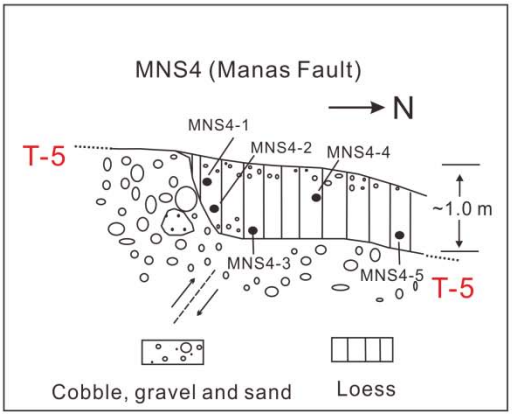
MNS4 (Manas Fault)
N
MNS4-1
MNS4-2
MNS4-4
T-5
~1.0 m
MNS4-3
MNS4-5
T-5
Cobble, gravel and sand
Loess

Figure 6

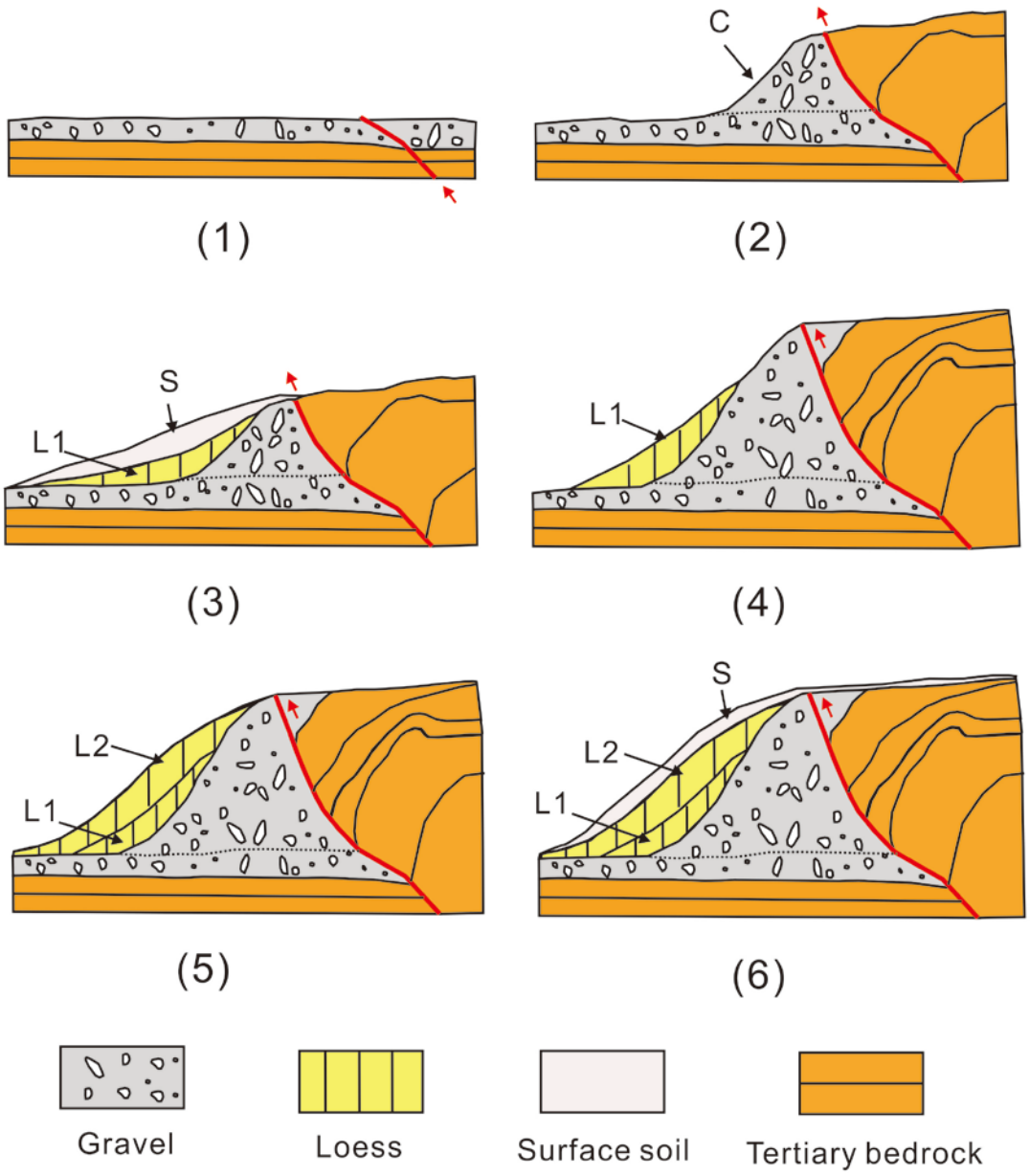
C
(1)
(2)
S
L1
L1
(3)
(4)
L2
L1
S
L2
L1
(5)
(6)
Gravel
Loess
Surface soil
Tertiary bedrock

Figure 7

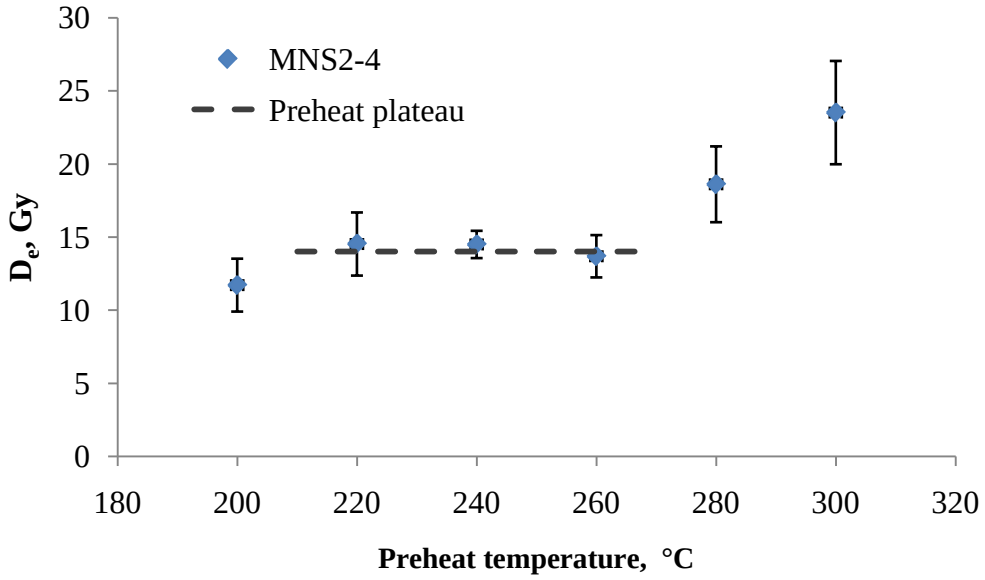
30
25
20
15
10
5
0
MNS2-4
Preheat plateau
De, Gy
180
200
220
240
260
280
300
320
Preheat temperature, °C

Figure 8

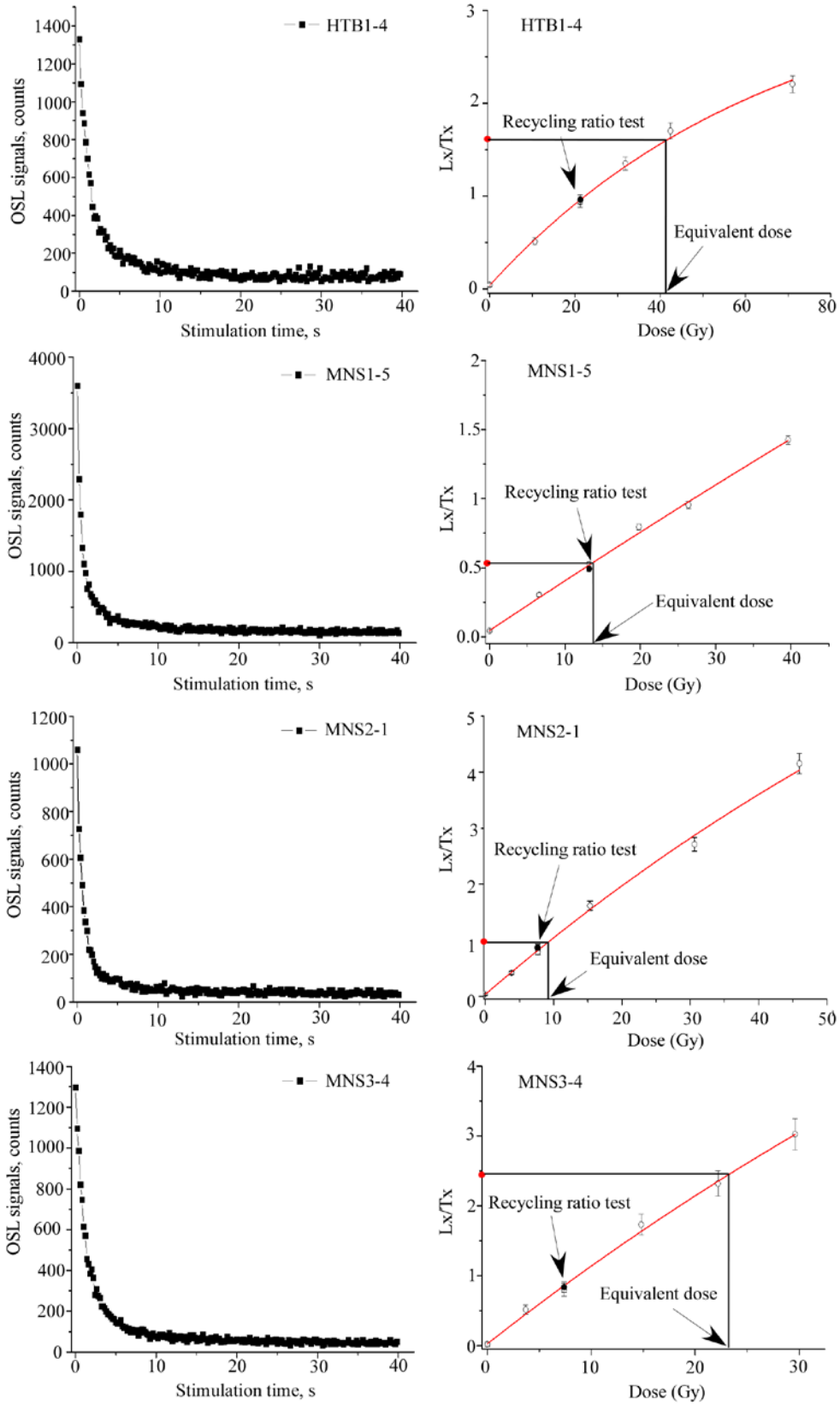
HTB1-4
OSL signals, counts
Stimulation time, s
HTB1-4
Recycling ratio test
Equivalent dose
Lx/Tx
Dose (Gy)
MNS1-5
OSL signals, counts
Stimulation time, s
MNS1-5
Recycling ratio test
Equivalent dose
Lx/Tx
Dose (Gy)
MNS2-1
OSL signals, counts
Stimulation time, s
MNS2-1
Recycling ratio test
Equivalent dose
Lx/Tx
Dose (Gy)
MNS3-4
OSL signals, counts
Stimulation time, s
MNS3-4
Recycling ratio test
Equivalent dose
Lx/Tx
Dose (Gy)

Figure 9

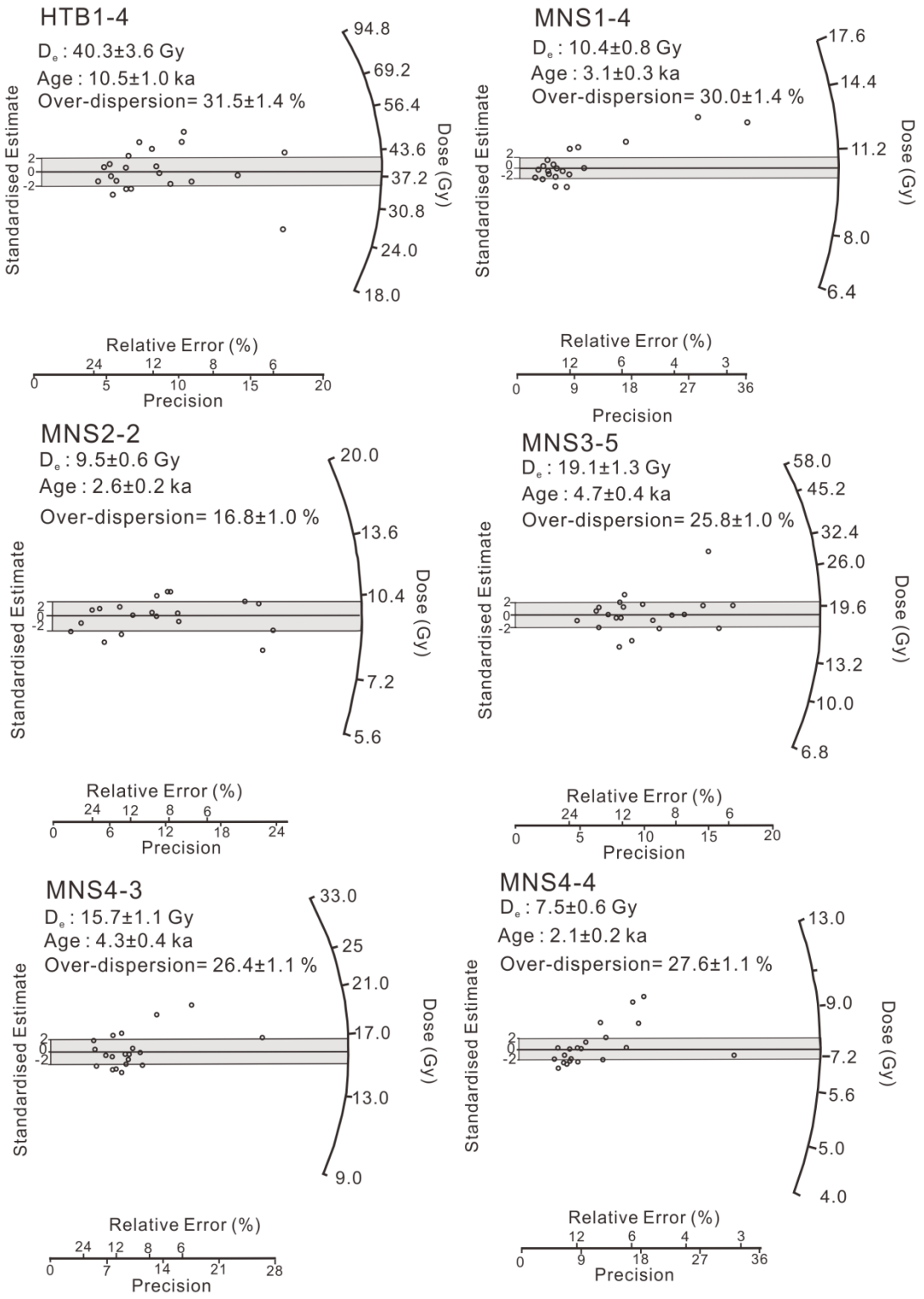
HTB1-4
De : 40.3±3.6 Gy
Age : 10.5±1.0 ka
Over-dispersion= 31.5±1.4 %
Standardised Estimate
Dose (Gy)
94.8
69.2
56.4
43.6
37.2
30.8
24.0
18.0
Relative Error (%)
24 12 8 6
0 5 10 15 20
Precision
MNS1-4
De : 10.4±0.8 Gy
Age : 3.1±0.3 ka
Over-dispersion= 30.0±1.4 %
17.6
14.4
11.2
8.0
6.4
Relative Error (%)
12 6 4 3
0 9 18 27 36
Precision
MNS2-2
De : 9.5±0.6 Gy
Age : 2.6±0.2 ka
Over-dispersion= 16.8±1.0 %
20.0
13.6
10.4
7.2
5.6
Relative Error (%)
24 12 8 6
0 6 12 18 24
Precision
MNS3-5
De : 19.1±1.3 Gy
Age : 4.7±0.4 ka
Over-dispersion= 25.8±1.0 %
58.0
45.2
32.4
26.0
19.6
13.2
10.0
6.8
Relative Error (%)
24 12 8 6
0 5 10 15 20
Precision
MNS4-3
De : 15.7±1.1 Gy
Age : 4.3±0.4 ka
Over-dispersion= 26.4±1.1 %
33.0
25
21.0
17.0
13.0
9.0
Relative Error (%)
24 12 8 6
0 7 14 21 28
Precision
MNS4-4
De : 7.5±0.6 Gy
Age : 2.1±0.2 ka
Over-dispersion= 27.6±1.1 %
13.0
9.0
7.2
5.6
5.0
4.0
Relative Error (%)
12 6 4 3
0 9 18 27 36
Precision

Figure 10

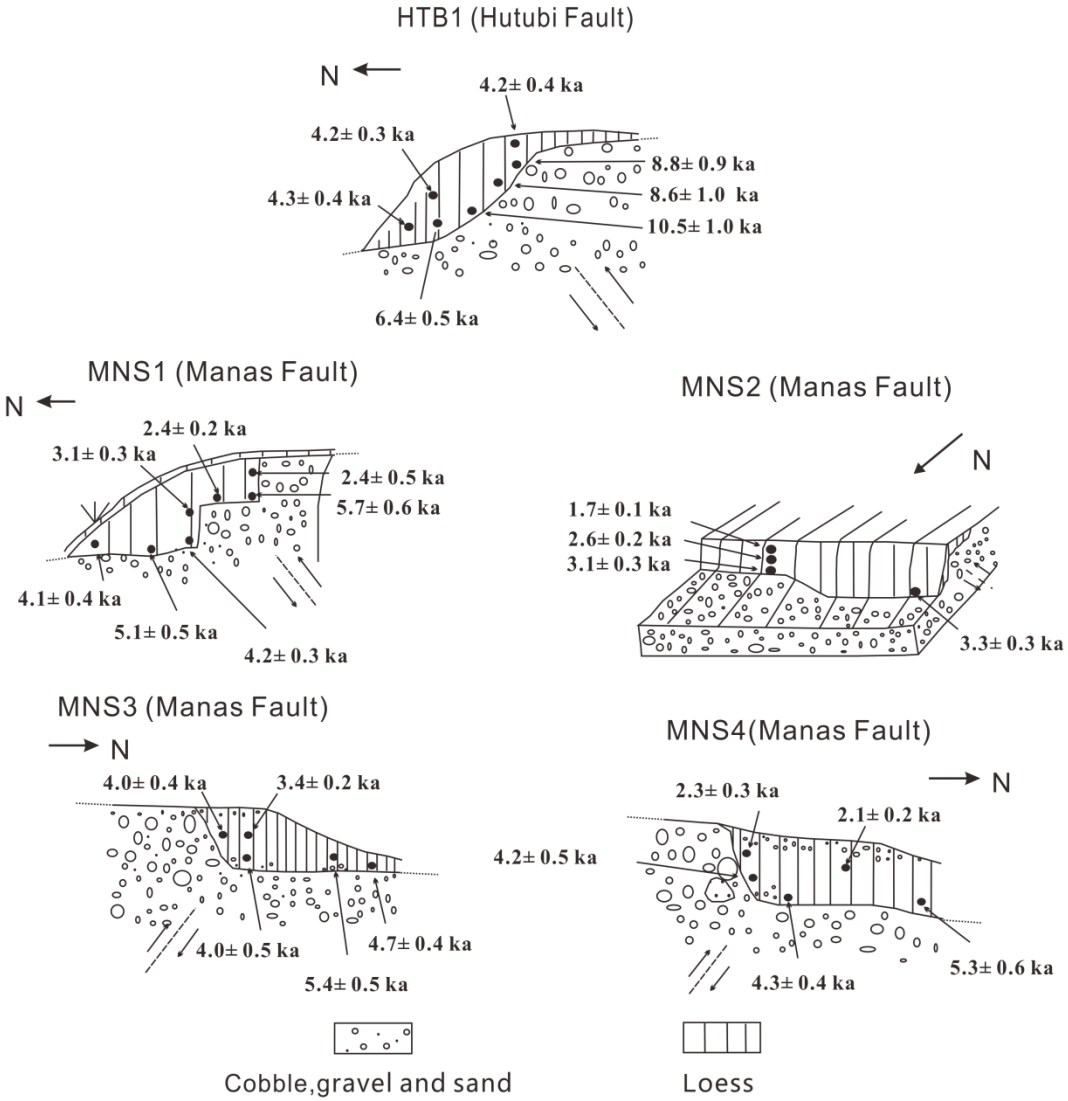
HTB1 (Hutubi Fault)
N
4.2± 0.4 ka
4.2± 0.3 ka
8.8± 0.9 ka
4.3± 0.4 ka
8.6± 1.0 ka
10.5± 1.0 ka
6.4± 0.5 ka
MNS1 (Manas Fault)
N
2.4± 0.2 ka
3.1± 0.3 ka
2.4± 0.5 ka
5.7± 0.6 ka
4.1± 0.4 ka
5.1± 0.5 ka
4.2± 0.3 ka
MNS2 (Manas Fault)
N
1.7± 0.1 ka
2.6± 0.2 ka
3.1± 0.3 ka
3.3± 0.3 ka
MNS3 (Manas Fault)
N
4.0± 0.4 ka
3.4± 0.2 ka
4.0± 0.5 ka
4.7± 0.4 ka
5.4± 0.5 ka
MNS4(Manas Fault)
N
2.3± 0.3 ka
2.1± 0.2 ka
4.2± 0.5 ka
5.3± 0.6 ka
4.3± 0.4 ka
Cobble,gravel and sand
Loess